NTNU
Det skapende universitet

# Karakterisering av magnetiske egenskaper til (111)-orienterte funksjonelle grensesjikt basert på komplekse oksider

**Fredrik Kjemperud Olsen**

Nanoteknologi
Innlevert: februar 2015
Hovedveileder: Thomas Tybell, IET
Medveileder: Ingrid G. Hallsteinsen, IET

Norges teknisk-naturvitenskapelige universitet
Institutt for elektronikk og telekommunikasjon

# Abstract

Interface engineering of functional materials is an emergent field with promising opportunities for device applications. Complex oxide materials exhibit a versatile range of functional properties, which make them particularly interesting for this purpose. In epitaxial thin films of complex oxides, crystal orientation, like (111), are rather unexplored and may exhibit novel functional phases compared to the more common (001)-orientation.

Magnetic properties of epitaxial heterostructures of ferromagnetic $La_{0.7}Sr_{0.3}MnO_3$ (LSMO) and antiferromagnetic $LaFeO_3$ (LFO) grown on (111)-oriented Nb-doped $SrTiO_3$ (Nb:STO) substrates have been investigated by vibrating sample magnetometry (VSM). Comparison of the (111)-oriented samples has been done with similar heterostructures in the (001) and (110)-orientation. The different layer configurations investigated are: LSMO / Nb:STO, LFO / LSMO / Nb:STO and LSMO / LFO / Nb:STO.

LSMO thin films on Nb:STO with varying thickness (2.3 - 21 nm) indicate the volume magnetization to be lower than reported for (001) oriented thin films. Coercive field values are found to be significantly lower than (001)-oriented films, but to have no specific trend with film thickness. Indications of a magnetic dead layer of similar thickness as reported in the (001)-orientation are found. Hystereses obtained show a shift along the field axis upon high field magnetization. This exchange bias effect is for all thicknesses found to be of similar magnitude, be reversible, and the extent of the shift to be dependant on magnetization field strength.

Heterostructures of LFO / LSMO / Nb:STO with 4 nm LFO layer on top and varying LSMO layer thickness (4 - 21 nm) are found to yield an increase in volume magnetization relative to the LSMO / Nb:STO samples. The increase is found to be enhanced, and accompanied by increase in curie temperature and coercive fields when the LSMO layer is thin (4 nm). An exchange bias with similar behaviour as seen in the LSMO / Nb:STO samples is observed for the samples with thickest (7 - 21 nm) LSMO layer, but not for the sample with 4 nm LSMO layer.

Heterostructures of LSMO / LFO / Nb:STO with a 4 nm LSMO layer and varying LFO layer thickness(2 - 21 nm) are also found to have an increase in volume magnetization, coercive field and curie temperature. The increase in moment and curie temperature is found to be highest with thin LFO layers (2 & 4 nm), but the coercive field values do not show a trend with LFO thickness. The observed effects have not been reported in other crystal orientations. Hence the interface environment in the (111) hexagonal crystallographic structure indicates to be inducing novel properties to the functional phases in possibly both material layers.

## Sammendrag

Grenseflater i funksjonelle materialer er et voksende forskningsfelt med lovende utsikter for anvendelse i elektronikk. Oksidmaterialer utgjør et bredt spekter av funksjonelle egenskaper som gjør dem spesielt interessante for dette formålet. I de forskjellige materialsystemene har spesielle krystallorienteringer som f.eks (111) særegne karakteristikker som gjør at de kan skape uvanlige funsksjonelle faser.

Magnetiske egenskaper til epitaksielle heterostrukturer av ferromagnetisk $La_{0.7}Sr_{0.3}MnO_3$ (LSMO) og antiferromagnetisk $LaFeO_3$ (LFO), grodd på (111)-orientert Nb-dopet $SrTiO_3$ (Nb:STO) substrater har her blitt utforsket ved bruk av vibrerende-prøve-magnetometer (VSM). Resultater fra de (111)-orienterte prøvene vil bli sammenliknet med liknende heterostrukturer i (001)- og (110)-orienteringer. De forskjellige konfigurasjonene av epitaksielle lag er: LSMO / Nb:STO, LFO / LSMO / Nb:STO og LSMO / LFO / Nb:STO.

Tynnfilmer av LSMO grodd på Nb:STO med varierende tykkelse (2.3 - 21 nm) viser en lavere magnetisering enn det som er rapportert i (001)-orientering. Verdier av koersitive felt er blitt funnet å være betydelig lavere enn i (001)-orientering, men å ikke vise noen spesifikk trend med tykkelse. Indikasjoner på et magnetisk dødt lag av lik tykkelse som rapportert i (001)-orientering er blitt funnet. Hystereser har blitt funnet å gi et skift langs den magnetiske felt-aksen. Denne forflytningseffekten er funnet å være av lik størrelsesorden og være reversible for alle filmtykkelsene, og mengden forskyvning er funnet å avhenge av styrke på magnetiseringsfelt.

Heterostrukturer av LFO / LSMO / Nb:STO med 4 nm LFO-lag på toppen og med varierende tykkelse av LSMO-lag (4 - 21 nm) er blitt funnet å gi en økning i magnetisering, i forhold til LSMO / Nb:STO-prøvene. Økningen er blitt funnet å være forsterket og akkompagnert av økt curie-temperatur og koersitive felt når LSMO-laget er tynt (4 nm). En forflytningseffekt med lik oppførsel som sett på LSMO / Nb:STO-prøvene er blitt funnet i prøvene med tykkes (7 - 21 nm) LSMO-lag, men ikke i prøven med 4 nm LSMO.

Heterostrukturer av LSMO / LFO / Nb:STO med 4 nm LSMO-lag og varierende tykkelse på LFO-lag (2 - 21 nm) er også blitt funnet å gi en økning i magnetisering, kohersitivt felt og curie-temperatur. Økningen i moment og curie-temperatur er høyest for prøvene med tynnest LFO-lag (2 - 4 nm), men verdiene for kohersitivt felt viser ingen spesiell trend med tykkelse. Disse observasjonene har ikke blitt rapportert tidligere i andre krystallorienteringer. Det virker dermed som at et annerledes miljø ved grenseflatene i (111)-orienteringen induserer nye egenskaper til de funksjonelle fasene, muligens i begge materialer.

# Preface

This thesis has been done with the oxide group at the Department of Electronics and Telecommunications, NTNU , in the period from Sep. 8. 2014 to Feb. 1. 2015, as my final project in a 5-year integrated masters degree in Nanotechnology. The work has been a continuation of my semester project done in fall semester 2014 [1]. Experimental work has been conducted at the laboratories of the institute.

Magnetic measurements have been done with a newly installed Vibrating sample magnetometer, which has had a number of teething problems. Some distracting situations with measurements, like sample holders which have given a magnetic response, or numerous hangups in the instrument software, has caused some slowing down to the progress. However good response from technical assistance has provided quick recovery and assured the project completion.

In most of the samples measured, a magnetic phase with unknown origin has been observed along the way. It was for long thought to be occurring due to noise from the instrument during measurements, and was thus regarded to give an uncertainty to the result values. But recently an annealing procedure done to one of the samples revealed that it could be reduced. A systematic investigation of the phase is currently ongoing, but the results are not in time for this thesis.

I would like to address special thanks my supervisors Thomas Tybell and Ingrid Hallsteinsen, who have been fabulously supportive throughout the whole project. I am sincerely grateful for inputs, guidance, feedback, discussion and support, which have given me tremendous motivation. I would also like to thank Magnus Moreau, Erik Folven and Jostein Grepstad for all interesting and motivating talks, and also a thanks to the rest of the oxide group, who all constitute to a stimulating working environment.

Fredrik Kjemperud Olsen
MTNANO
NTNU, Trondheim
January 31, 2015

# Contents

# 1. Introduction

## 1.1 Motivation

While for many years device technology has been based on semiconductor materials being the main ingredient in electronic products [2], focus has lately increased in complex oxide materials research, much due to recent advancement in synthesis technologies [3]. Oxide materials are known to exhibit a range of functional properties, which offers opportunities for multifunctional devices [4]. As device designs are constantly being pushed towards smaller dimensions, nanosize effects are introduced and eventually lead to the materials losing their bulk properties. On the other hand, other eminent properties emerge when the materials reach the smallest dimensions. Increased research on oxide heterostructures has lead to discovery of novel phenomena exhibited by layers on atomic scale [5], and focus on the material interfaces themselves has boomed due to discovery of functional phases that occur only in their vicinity [3]. A particularly interesting class of oxide materials is the perovskites.

Perovskites are a versatile class of materials. With the chemical formula $ABO_3$, they can hold many elements in the periodic table, which is one of the reasons why they exhibit a large range of various properties. Some of the most commonly know functional properties are ferroelectricity ($PbTiO_3$), piezoelectricity($Pb(Zr,Ti)O_3$) [6], ferromagnetism ($SrRuO_3$, $La_{1-x}Sr_xMnO_3$) [7] or colossal magnetoresistance ($La_{1-x}Sr_xMnO_3$, $Pr_{0.7}Sr_{0.04}Ca_{0.26}MnO_{3-\delta}$) [4, 8]. Some even have coexistence of different functional phases like multiferroicity ($BaTiO_3$,$FeTiO_3$) [4, 9]. For many of these perovskites it it is relatively easy to induce transitions between the different phases, for instance metal-insulator transitions which is a central functionality in modern electronic applications. The functional properties in perovskites are highly coupled to the crystal structure [3], which makes epitaxial systems especially interesting since one may induce strain and distortions, and hence ultimately tailor the functional properties. Since different perovskites have different properties but share the same crystal structure, they may to high extent be designed together.

## 1.2 Background

Ferromagnetic and half-metallic $La_{1-x}Sr_xMnO_3$ (LSMO) and antiferromagnetic and insulating $LaFeO_3$ (LFO) are two perovskite materials which have had intensive study as epitaxial systems, for instance grown on $SrTiO_3$ (STO) [10–12]. However research has mainly been in (001) and (110)-orientated systems, and little has been done in the (111)-orientation. Recent development of growth techniques by pulsed laser deposition (PLD) has enabled high quality epitaxial films of (111) LSMO and LFO on STO [13]. Termination by (111)-planes gives a different surface chemistry than the (001) and the (111)-orientation, and the (111)-planes also have a hexagonal symmetry, in contrast to the cubic and tetragonal (001) and (110)-orientations. These differences are believed to yield novel results. For instance is LFO fully spin polarized in the (111)-plane [14], which could lead to a different coupling to the ferromagnetic LSMO layer than in the other orientations. Also, the orientation may yield different structure distortions to the layers at the interface, which could alter the electronic and magnetic properties differently than in the (001) and (110)-orientations. As the LFO / LSMO heterostructure is not known to have been studied in the (111)-orientation, investigation of this system is considered highly interesting.

## 1.3 Outline

This thesis consists of six chapters. After this introduction, chapter 2 will have a short introduction to magnetism theory in solid materials, with focus on ferro- and antiferromagnetism. Then chapter 3 will explain some state of the art prospects of perovskite materials, especially reported findings and predictions for epitaxial systems of LSMO, LFO and STO. Chapter 4 covers the experimental part, where the sample preparations and measurements are explained. In chapter 5 the results will be presented in a structural manner, and discussed along the way. The conclusions are summarized in chapter 6.

# 2. Theory

## 2.1 Atomic Magnetism

*This section covers a brief introduction to the origin of magnetic moments in electron spins, and how electron distributions in atomic orbitals may give rise to magnetic properties of materials.*

### 2.1.1 The electron spin

Magnetism is a phenomena that presents itself where there is a circular motion of charge, and in solid materials it is closely related to the presence of unpaired electrons. On this microscopic level, it is still circular motion of charge that generates magnetic moments and fields. Electrons exert on their own what is commonly referred to as the electron spin. In addition, the electron orbits around the atomic nucleus, which gives rise to another magnetic moment contribution, referred to as the orbital angular momentum. These magnetic moments induce a magnetic field with a direction dependant on the circular motion. The circular current in figure 2.1 has a counter-clockwise direction observed from above, but a clockwise direction from below, and hence magnetic fields are labelled to have a north and a south pole as indicated in the figure. There are consequently only magnetic dipoles, and no monopoles.

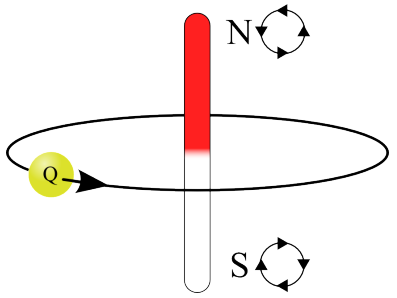


**Figure 2.1:** Magnetic field induced by circular motion of a charge Q around an axis. North (N) and south (S) poles are indicated lying on the axis of rotation. The projection of the charge motion as seen from the respective poles are indicated by small circles.

### 2.1.2 Quantification of the spin

When doing macroscopic experiments with magnetic materials, one would want to link the macroscopically measured moments to the microscopic electrons in the material. A single electron can be considered a cluster of negative charge spinning around an axis. Electron spin moments may then be calculated in Bohr magnetons, $\mu_B$, defined as

$$\mu_B = \frac{eh}{4\pi mc} \approx 9.274\,009\,68 \times 10^{-21}\,\mathrm{erg/G} \tag{2.1}$$

where *e* is the electron charge, *h* is Planck's constant, *m* the electron mass and *c* the velocity of light. The spin moment $\mu_s$ from a single electron is

$$\mu_s = g\sqrt{s(s+1)}\mu_B \tag{2.2}$$

where $g$ is the gyromagnetic ratio (also called $g$-factor) which has a value close to 2, and $s$ is the spin quantum number $\frac{1}{2}$. Solving $\mu_s$ with these values gives $\mu_s \sim 1.73\mu_B$. For an atom or ion that has a non-zero number of unpaired electrons, the total spin moment summed up is given by

$$\mu_S = g\sqrt{S(S+1)}\mu_B \tag{2.3}$$

where $S$ is the sum of the spin quantum numbers from all electrons. When electrons pair up in an atomic orbital state, they take opposite spin quantum numbers $s$, so for instance in an atom with all electrons paired up, $S$ would be zero and there would be no magnetic moment.

In addition, $L$ is the orbital angular momentum quantum number and may be taken into calculations. In materials however, the orbital momentum contribution for an electron may be severely quenched by the electric field from the crystal lattice. The field pins the orbital motion, and restricts its ability to change under an external magnetic field [15].

### 2.1.3 Quantum mechanic electron states in atoms

The positions and motions of electrons in atoms are explained by quantum mechanics. The quantum states for electrons in atomic orbitals are found by solving the Schrödinger equation, which assigns the electron with three integer quantum numbers: $n$, $l$ and $m_l$, and the spin quantum number $s$ which may have values $+\frac{1}{2}$ or $\frac{1}{2}$. These quantum numbers models and explains the placement of electrons in electron shells, orbitals and the orientation and magnitude of their magnetic contributions [16].

The different quantum states for electrons in an atom have different energy. $n$ separates the electron energies in levels according to the shells $E_n$, where the energy increases with $n$ as indicated in figure 2.2. However all electrons within one shell do not have the same energy. Since the orbitals are differently oriented in space, electrons experience different effective nuclear charge. This results in the states in the outer orbitals within a shell having additional increased energy, indicated by $l$ in figure 2.2. In addition when a field is present, each magnetic moment *m* gains an energy *E* given by

$$E = -\boldsymbol{m} \cdot \boldsymbol{H} \tag{2.4}$$

As there are two origins of magnetic moment from an electron, and the orbital magnetic moment about a field axis may be expressed as $\boldsymbol{m} = -\mu_B m_l$, the electrons gain an additional energy when exposed to an external field:

$$E = \mu_B m_l H \tag{2.5}$$

Here, it is clear that the electron energy in a magnetic field depends on $m_l$, and the relation indicates how the total energy of an electron will change under an applied field. This is known as the Zeeman effect [17], and shown in figure 2.2.

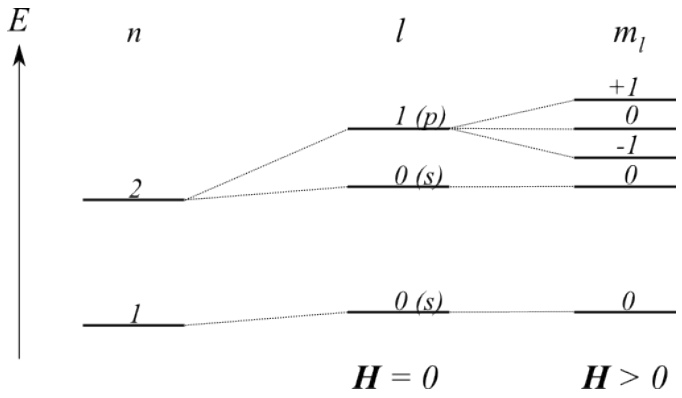


**Figure 2.2:** Electron energy levels and Zeeman effect. Reproduced from [18]

In an orbital which is partly filled, the electrons will feel electrostatic repulsion from each other, making them spread out as much as possible in space, and this is the foundation of what is known as Hund's rules - which explain how parallel spins and thus magnetic moments are established on an atomic scale. Hund's rules are covered in previous work [1].

## 2.2 Band Magnetism

*While the atomic interpretation allows us to to better describe the electron distributions and magnetic momenta in atoms, when atoms merge to form crystals and solid materials the situation is altered. This section starts out with explaining classic classification of magnetic ordering phenomena, then more in depth how different magnetic phases occur in solid state materials - with emphasis on ferromagnets and antiferromagnets.*

### 2.2.1 Classification of magnetic materials

In solid materials the orbital states from each individual atom hybridize together to form bands - a quasi-continuum of states. Since electrons in solid materials pair up in states with antiparallel spins in accordance with the *Pauli exlusion principle* [18], it implies that a material has to have only partially filled bands for it to be magnetic - two paired electrons will cancel out each others magnetic moment. Thus most magnetic solids are compounds of transition metals or lanthanides which have partly filled $d$ and $f$ bands respectively. Although the physics of the different ordering phenomena that arise on this microscopic level are complex, their results are easily observed through different magnetic response behaviour on a macroscopic level and have thus been classified according to these. Figure 2.3 visualizes the different ordering behaviours.

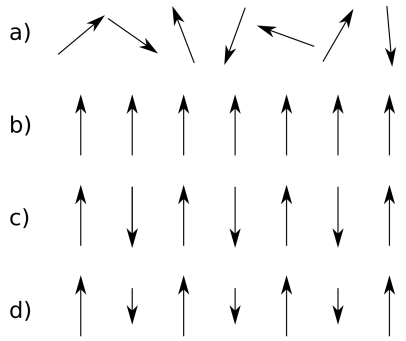


**Figure 2.3:** Magnetic ordering in different classes - a) Paramagnetic, b) Ferromagnetic, c) Antiferromagnetic and d) Ferrimagnetic. Reproduced from [1].

*Paramagnetic* ordering has a random distribution of the magnetic moments throughout the crystal, giving a net zero moment. This occurs in materials where the electron interactions are weak. When the interactions are stronger, different cooperative magnetic phenomena may occur. The magnetic moments may align parallel in which case the material becomes *ferromagnetic* and exert a net magnetic moment, or antiparallel in which case it is *antiferromagnetic* and have no net moment. Antiferromagnets have the same net moment in opposite directions, so the different contributions cancel each other out. *Ferrimagnets* also have antiparallel ordering, but the values in the two directions are not equal, resulting in a net magnetic moment [15].

### 2.2.2 Diamagnetism

All materials show a so-called diamagnetic response, i.e. that they under the influence of an external applied magnetic field will appear as to be inducing an opposing field. However the effect is very weak and may be overlooked when other, stronger phenomena are present. Thus even though all materials exert diamagnetism, only the ones that do not have a stronger magnetic phenomena present are classified as diamagnetic. The diamagnetic response happens due to change in the orbital motion of electrons, and will happen whether the orbitals or bands are filled or not. In electromagnetic theory, when an external field is applied to an electric circuit, currents are induced opposing the applied field according to Lentz law [19]. The same happens for atoms, but it is the electron orbital motions that are altered in the way that they induce more current flow resulting in a magnetic field opposite to the external one. In other words the *magnetic susceptibility* $\chi$ of diamagnetic materials is negative, by that the response is an induced opposite field [20].

### 2.2.3 Paramagnetism

For materials that have unpaired electrons, the magnetic properties become stronger than that of the diamagnetic. For such materials the interaction between the separate atoms become decisive, and where it is sufficiently weak, thermal energy can cause the magnetic moments to fluctuate randomly. In this case, the material is classified as paramagnetic. In the absence of an external field paramagnets therefore have no net moment. However in contrast to diamagnets they have a small positive susceptibility, and in the presence of an external magnetic field the individual spin moments will start to align with the field direction, causing a net moment. When the field is removed, the material returns to the randomly ordered state. In many materials, a certain thermal energy is necessary to overcome the spin interactions. Under this certain temperature, called the *Curie temperature*, the material becomes ferromagnetic. The susceptibility in paramagnetic materials close to the transition temperature may be modelled by the Curie-Wiess law

$$\chi = \frac{C}{T - T_C}, \qquad C = Nm^2/3k_B \tag{2.6}$$

where $N$ is the number of magnetic moments $m$ per volume and $T$ is the temperature. $T_C$ is the material specific Curie temperature [18].

### 2.2.4 Ferromagnetism

In ferromagnetic materials there are strong interactions between the individual magnetic moments, causing long range order and spontaneous magnetization. This interaction may be modelled by an *exchange field* $B_E$ which acts on the individual magnetic moments, and is proportional to the magnetization of the material.

$$B_E = \lambda M \tag{2.7}$$

The proportionality factor $\lambda$ is related to the Curie temperature by

$$\lambda = \frac{T_C}{C} \tag{2.8}$$

The exchange field is a measure of how strong the aligning interactions are, and may be orders of magnitude stronger than the magnetic field - for instance with iron $B_E \approx 10^3$ T [21]. This means that a very strong magnetic field would have to be applied to break the parallel ordering.

It can be shown according to the *Heisenberg model* that parallel spin ordering may be predicted for a material by the *exchange integral* $J$. $J$ is quantum mechanical in nature, and has no classical equivalent [18]. But it is related to the overlap of charge distributions on individual atoms, and will indicate whether the electron distributions will favour parallel or antiparallel ordering. The energy from exchange interactions may be modelled by

$$U = -J\mathbf{S}_i \cdot \mathbf{S}_j \tag{2.9}$$

where S are the spins on atoms *i* and *j*. By this convention, for $J > 0$ a parallel order will be favoured, and for $J < 0$ antiferromagnetic ordering will be favoured [21].

**Collective electron theory**

In ferromagnetic metals, since electrons are not localized on separate atoms but in energy bands, the localized moment theory breaks down. Two effects from this are especially observed. a) Moments measured in ferromagnetic and paramagnetic phases are not equal, as they should be according to Weiss theory, b) each atom's moment does not correspond to an integer number of electron spins [18]. This is explained by the energy and density of states for the electrons in the partially filled bands. In bands, the interaction which promotes parallel aligned spins within a band is in general the same as the one in atomic orbitals - explained by exchange energy. However in bands, the density of states is important. While $s$ and $p$ bands are broad in energy, they have a low density of states which means that the exchange energy has a steep increase for each electron which is promoted. The $d$ band is however more narrow in energy but has a larger density of states, so more electrons are close to the fermi level and may be promoted by little energy to higher states. The high density of electrons reduces the energy cost to reverse a spin, and the exchange effect prevails. The effect, causing ferromagnetism in transition metals, can be visualized by dividing the states in the bands by spin up and spin down and including the exchange energy - as shown in figure 2.4.

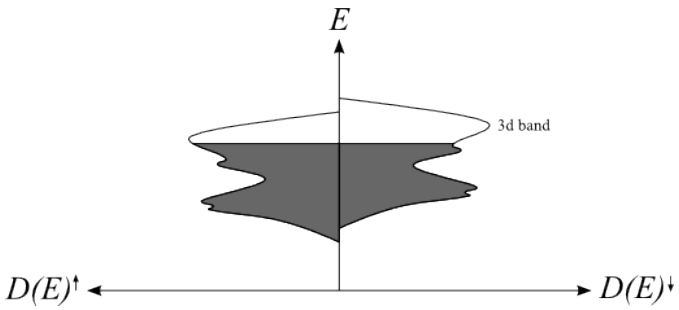


**Figure 2.4:** Visualization of spin up and spin down density of states of a partially filled $3d$ band in transition metals. The exchange interaction is included, causing the shift along the energy axis. Reproduced from [18].

### Domain Theory

Even when parallel spins are favoured energetically on a microscopic level, the ordering does not necessarily extend through the whole material, and macroscopically the observed magnetic moments may be less than the predicted saturation moment. This is because the material consists of regions called *domains* where the magnetization is saturated within, but different domains do not necessarily have the same direction. An example of domains is shown in figure 2.5.

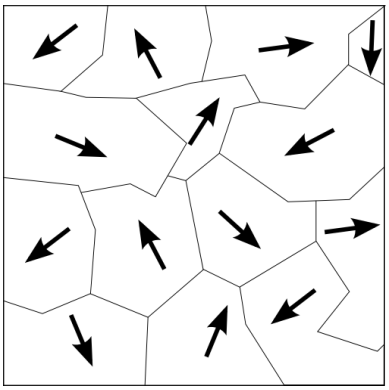

**Figure 2.5:** Example of domain structure in ferromagnetic materials. Each arrow indicates the magnetization direction within the individual domains.

Domains occur due to magnetostatic energy that arises when two magnetic dipoles are in vicinity of each other. The *demagnetization field* from one causes the other's presence to cost energy. From equation 2.4 one can see that when the dipole is oriented parallel with a field, the energy is negative, while it is positive when oriented antiparallel. The demagnetization field from a dipole is not uniform in space, as seen in figure 2.6. This causes parallel oriented dipoles to have positive or negative magnetostatic energy depending on where they are located in the demagnetization field.

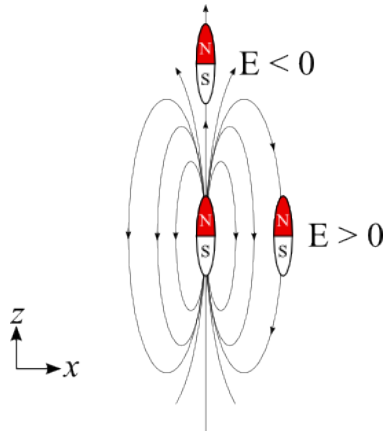


**Figure 2.6:** Schematic of the energy cost of aligning dipoles in different spatial orientation relative to one dipole's demagnetization field.

If the dipole with positive energy in figure 2.6 was to flip around, it would lower its magnetostatic energy relative to the demagnetization field. But it would not be oriented parallel with the other dipoles anymore. A similar effect causes domains of different oriented moments to occur in ferromagnets - the different orientations happen because the material as a whole lowers its magnetostatic energy.

All energy terms are however not lowered with domain formation. At the boundaries between domains, called *domain walls*, the dipoles are not oriented parallel, and domain walls therefore cost energy. Hence the formation of domains is only energetically favourable as long as the gain from lowered magnetostatic energy is higher than the energy cost of the domain walls, and the energy balance effectively controls the size and distributions of domains. One can understand the formation of different domains by following the structures in figure 2.7.

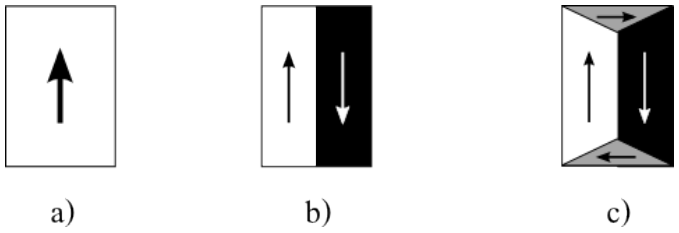


**Figure 2.7:** Establishment of domains - Reproduced from [21].

An imagined establishment of domains is followed from left to right in figure 2.7. In a), a single domain generates a demagnetization field which gives itself a magnetostatic energy. In b) the energy is lowered due to the formation of a second domain with antiparallel oriented moment. In c) the formation of two additional domains with moments aligned with the demagnetization field lowers the energy to zero. These domains are so-called *closure domains* due to that they complete the magnetic flux circuit within the crystal [21].

### Domain walls

At the boundary between two domains, the moment direction change is not abrupt, but a gradual rotation occurs over a distance. A stepwise moment rotation effectively lowers the exchange energy that is created. In bulk ferromagnetic materials the typical domain wall is of a type called *Bloch wall*, shown in figure 2.8. Domain walls tend to follow the transition pattern which yields least energy cost. The Bloch wall is one of such, where the moment directions rotate around and axis perpendicular to the boundary through the whole transition [18].

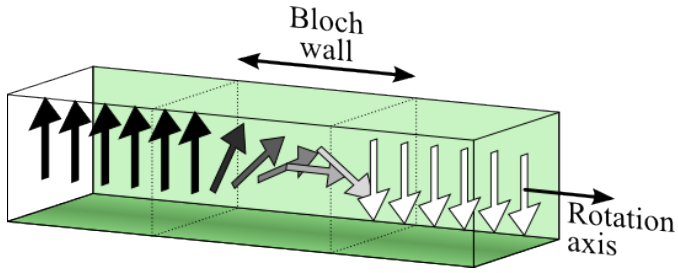


**Figure 2.8:** Dipole orientations through a Bloch wall - Reproduced from [18].

### Magnetocrystalline energy

The energy of a domain wall may be modelled to consists of two dominant factors - the exchange energy and anisotropic energy. The anisotropic energy, also called *magnetocrystalline energy*, originates from the fact that magnetic dipoles in crystals have an energy which is lowered along certain crystallographic directions called *easy axes* [21]. It is highly coupled to the crystal structure of the material. Its origin can be understood by when dipoles rotate around in the crystal, the electron distributions rotate with them. This causes their overlap, and thus exchange energy and electrostatic interactions to change, making some directions require more energy than others since the crystal is not fully symmetrical. This is observed on a macroscopic scale, where magnetizing a ferromagnetic sample is easier along certain crystallographic directions. Different observable macroscopic behaviour is shown in the hysteresis curve in figure 2.9b.

### Hysteresis

In ferromagnetic materials, when an external field is applied, the domains oriented close to the field direction will grow at the expense of the ones least aligned, and when large fields are applied the direction of each domain also start to rotate towards the field direction. These two contributions are slightly different. While the domain direction rotation will reverse when the field is removed, growth of domains is an irreversible process. The induced permanent change in the domain structure causes ferromagnets to show hysteresis behaviour, shown in figure 2.9a.

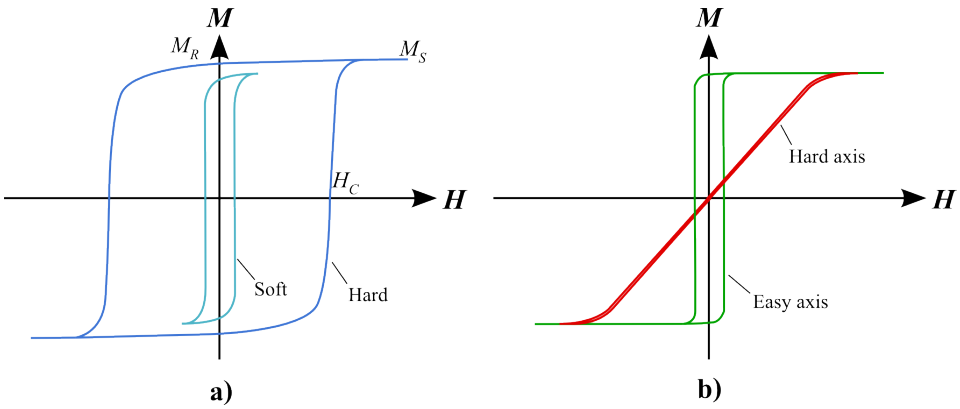


**Figure 2.9:** Hysteresis behaviour from ferromagnets. a) Hysteresis with common attributes as explained in the text. The thinner hysteresis indicates the distinction between hard and soft ferromagnets. b) Typical hysteresis behaviour along easy or hard magnetic axes.

After a certain field strength, all domains will be parallel aligned, at the point where the induced magnetic moment in the material saturates - $M_S$. The irreversible change done to the domains leads to a remnant magnetic moment after the field is removed - $M_R$, and an opposing field $H_C$, called the coercive field, is required to turn the magnetization back to zero. All the characteristics of a hysteresis loop is related to the domain architecture. Ferromagnets are labeled *hard* or *soft* from the magnitude of their coercive field. In hard magnets, more energy is required to change the domain structures and switch the magnetization. Soft magnets are on the other hand relatively easy to switch. The energy is related to microscopical movement of domain walls - in some materials they move more freely than others. Several factors may pin or restrict domain wall movement, in general changes which lead to local alternation of the energy terms relevant for domain wall movement - for example crystal defects. However domain walls do not necessarily lie along crystal grain boundaries, because their positions are primarily governed by magnetostatic energy.

### 2.2.5 Antiferromagnetism

In antiferromagnetic materials there are also strong interactions between the adjacent magnetic dipoles, but which lead them to align antiparallel. There are thus two ”subsets” of magnetic moments, which neutralize each other from a macroscopic viewpoint. This is not the same as when electrons are paired up and neutralize each others spins - the antiparallel ordering first occurs on a larger scale [20].

Most antiferromagnetic materials are compounds of transition metals and oxygen or sulphur. In these materials, the exchange integral $J$ between ions in the crystal is negative, favouring antiparallel ordering of the spins connected in the interactions. This leads to adjacent magnetic moments in the crystal aligning antiparallel and macroscopically no net magnetic moment is observed.

However it is impossible for a crystal to have antiferromagnetic order in all directions. As in ferromagnets, the anisotropy of the crystal structure influences the magnetic moments, and even though $J$ may be negative for interactions in all directions, it is higher in

some than others. This will cause parallel ordering along certain crystallographic directions where $J$ is the least negative [21]. A common way to classify antiferromagnets is by so-called *types* that tell which directions or planes have ferromagnetic ordering [14]. An overview of the most common types is shown in figure 2.10.

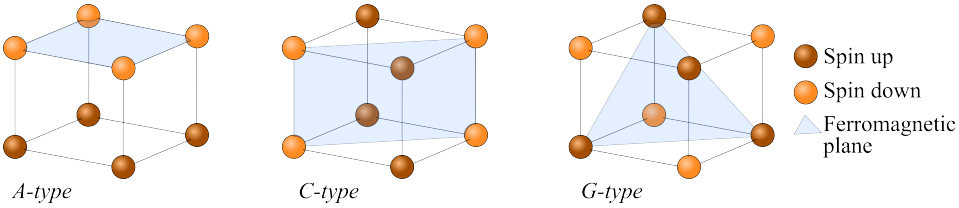


**Figure 2.10:** Different antiferromagnetic ordering types - Reproduced from [14]

Over a certain temperature called the Néel temperature $T_N$, the antiferromagnetic ordering is overcome by thermal energy and the material behaves paramagnetic. In the antiferromagnetic phase, they have a small positive susceptibility and exert no remnant magnetization after field exposure. This means that they appear like paramagnets macroscopically, and antiferromagnetic ordering in crystals was first proved experimentally by neutron diffraction methods, which revealed parallel ordering along certain crystal directions and thus showed the picture of two subsets. However if an external field is large enough, it will overcome the exchange energy and be able to flip both subsets in the field direction, causing all moments to align parallel. But this field can be quite high, as discussed on ferromagnets. An induced moment which may be seen at lower fields from antiferromagnets is generated by *spin cantering* [18], shown in figure 2.11. An applied field will rotate the individual moments towards the field direction, making them deviate from their preferred orientations. When the field is removed, the cantering effect reverses.

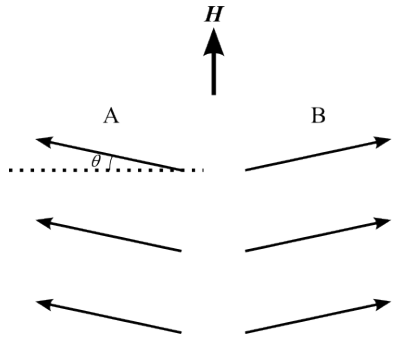


**Figure 2.11:** Spin cantering in antiferromagnets under an applied external field. Both sublattices A and B are effected by the perpendicularly aligned magnetic field, and rotate an angle $\Theta$ from their axis. Reproduced from [18]

### 2.2.6 Magnetic thin films

In magnetic thin films, the importance of anisotropy in the structure becomes important on the magnetic properties. Magnetic dipoles tend to deviate their orientation from bulk crystalline easy axes, and follow the surface plane instead. This can be understood by the material reducing its magnetostatic energy, in the same way as seen in figure 2.7, but in thin films the whole material behaves relatively like a surface. In ferromagnetic thin films, domain walls are typically found to be of a type called *Neél walls* - shown in figure 2.12.

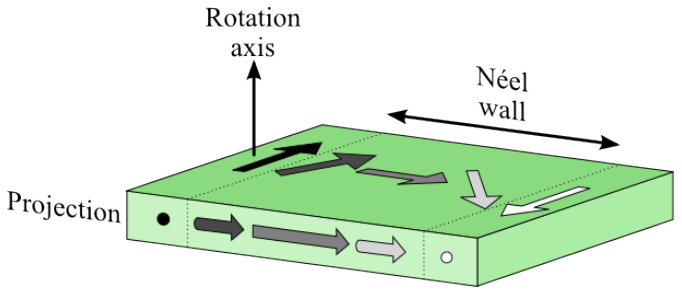


**Figure 2.12:** Dipole orientations through a Néel wall - Reproduced from [18].

In Neél walls the axis of moment rotation is not perpendicular to the domain boundary, but to the film surface instead. This is energetically favourable because keeping the moments in the surface plane keeps the magnetostatic energy low. However it induces new dipoles with components pointing out of the boundary plane, as indicated in figure 2.12 by projection of the dipole components in a plane perpendicular to the boundary. Despite this generation, a Néel wall still yields the lowest total energy for thin films. The balance between different energy terms related to dipole orentations in ferromagnetic thin films was described by Charles Kittel [22]. He found that the domain structure in thin films do not obey the structure shown in figure 2.7c under a certain critical film thickness, but that it becomes energetically favourable to have all dipoles in the surface plane. He also found that the size of domains in ferromagnetic thin films are proportional to the square root of the thickness [23]. This dependancy is known as the Kittel law.

# 3. State of the art

*In this chapter, a type of transition metal oxide materials - the perovskites - will be presented with focus on their functional properties as magnetic materials and thin films.*

## 3.1 Perovskites

To start off with interpretation of perovskites, its is important to understand their crystal structure. The unit cell of the cubic perovskite crystal structure is shown in figure 3.1.

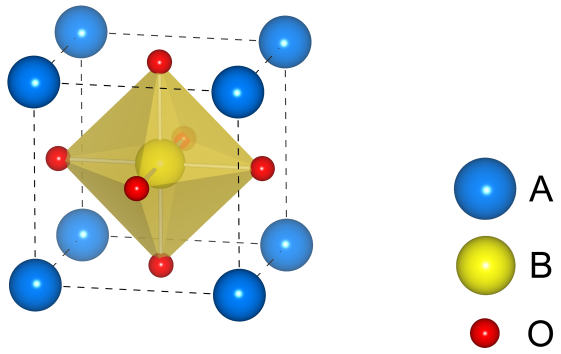


**Figure 3.1:** Unit cell of the cubic perovskite crystal structure

The B-cation's position is called an octahedral position because it is surrounded by eight oxygen anions, and the yellow faces that surrounding it make up what is called the octahedra.

### 3.1.1 Tolerance factor

Many perovskites do not show a fully symmetrical cubic structure like the one shown in figure 3.1. The variety of elements that can take the A and B lattice sites are not necessarily ideally sized for the $ABO_3$ framework, and thus the crystal may alter its symmetry. The Goldschmidt tolerance factor $t$ is an easily apprehensible indicator of such crystal deviations, and is directly derived from the radii of the A and B ions of a perovskite unit

cell [24]. It is though important to note that crystal structures are highly dependent on temperature as well, while its effect is not included in the tolerance factor. The tolerance factor gives the simple interpretation of its values $t = 1$ for cubic structure, and $t > 1$ or $t < 1$ for deviations.

$$t = \frac{r_A + r_O}{\sqrt{2}(r_O + r_B)} \tag{3.1}$$

Where the ionic radii are close to ideal sizes the cubic perovskites are found. For values $t > 1$, the the A-site cations are larger, which makes the octahedra become too large for the accommodating B-cation. This may cause B cation displacement, which can cause ferroelectric properties such as seen in tetragonal perovskites like $BaTiO_3$, $PbTiO_3$ or $KNbO_3$ [25]. When $t < 0.9$, the framework on the other hand around the octahedra becomes too unsupportive, and the octahedra begin to tilt to their sides. These so-called octahedral rotation distortions, which are shown in figur 3.2, are predicted to influence the electronic and magnetic properties of the compound [3, 26].

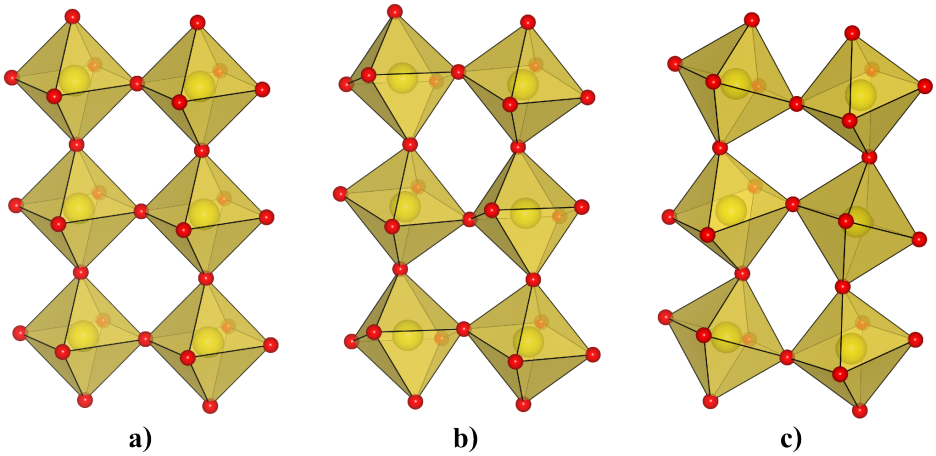


**Figure 3.2:** Examples of octahedral rotation distortions in perovskite structures a) Cubic (no distortions), b) Rhombohedral and c) Orthorhombic.

The electron distribution overlaps between the ions may be severely altered when the crystal undergoes these alternations [27]. This is one of the reasons why different magnetic properties are found in different perovskites, and why research on for instance doping effects have been prominent [3, 28].

### 3.1.2 Structural phase transitions

The picture is though not as simple as to just take the ionic radii into consideration. The crystal may undergo structural transformations with temperature. Temperature causes phonons in the crystal to become excited, and phonon dispersions are highly dependant on the crystal structure. The structure which yields the minimum free energy at a each

temperature $T$ will be the most stable and hence favoured. This may result in structural changes to occur as the material is exposed to different temperatures. As an example, $BaTiO_3$ is cubic above $393K$, shifts to tetragonal below this temperature, to orthorhombic below $273K$ and to trigonal at $183K$ [29]. Many perovskites have complex phase diagrams as function of temperature.

### 3.1.3 Crystal field splitting and Jahn Teller distortions

The ions giving rise to magnetic moments in perovskites are usually the B-cations. For transition metals situated in octahedral positions, the five degenerate $3d$ orbitals split into two energy levels - $t_{2g}$ and $e_g$. This splitting, called the *crystal field splitting*, occurs due to different orientations of the orbitals relative to the surrounding anions, hence some orbitals cause more overlap and have higher energy [20]. The orbitals are labeled $d_{xy}$,$d_{xz}$,$d_{yz}$,$d_{x^2-y^2}$ and $d_{z^2-r^2}$ due to their orientations in x, y and z directions. A visualization of the orbitals is given in figure 3.3. The figure shows how the $t_{2g}$ point towards the edges of the octahedra (middle between two oxygens) while the $e_g$ orbitals point directly towards the oxygen anions. This gives a simple interpretation of why the $e_g$ levels are higher in energy. The effect of the crystal field splitting on energy levels is shown in an example by the first separation in figure 3.4, where the $3d$ splits into $t_{2g}$ and $e_g$.

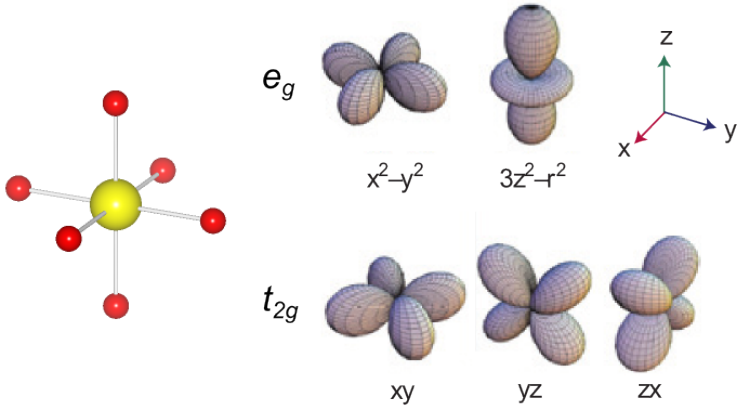


**Figure 3.3:** Orbital spatial extentions for transition metals in octahedral positions. Reproduced from [3]

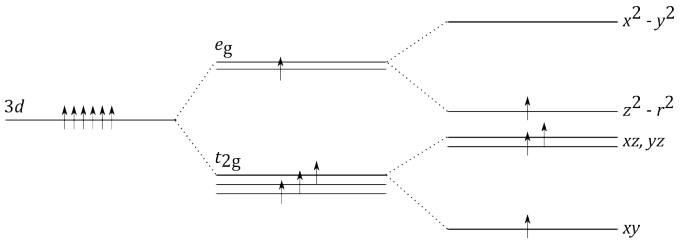


**Figure 3.4:** The splitting of the $3d$ orbitals of $Mn^{3+}$ in LSMO. The orbital first splits in two ($e_g$ and $t_{2g}$) due to crystal field splitting, then into four ($x^2 - y^2$, $z^2 - r^2$, $xz$, $yz$ & $xy$) due to Jahn-Teller distortions. Reproduced from [1]

Regarding exchange energy and electron pairing, all transition metals do not show the parallel ordering for all electrons like in figure 3.4. If one imagines placing the four electrons one by one into the orbitals, it is easy to place the first three - into $t_{2g}$. The reason why $Mn^{3+}$ then has its fourth electron placed into $e_g$ and not paired with one in $t_{2g}$ is because the field splitting between $t_{2g}$ and $e_g$ is lower than the pairing energy. The $t_{2g}^3$ $e_g^1$ configuration which occurs in $Mn^{3+}$ is called *high spin* (HS), while some metal cations takes $t_{2g}^4$ $e_g^0$ which is called *low spin* (LS). In general, the extent of crystal field splitting differs for materials, and this causes different ordering. Transition metals with $3d^4$ high spin state have more magnetic moment than those with low spin because the sum of spin moments *S* is either 4 or 2 [20].

Another distortion effect called *Jahn Teller distortions* arises when the $e_g$ orbitals are unequally filled, which is the case for some transition metal cations such as for instance $Mn^{3+}$. An electron placed in one of the two $e_g$ orbitals (for instance $z^2 - r^2$) will have high energy since it is located close to an oxygen anion, and this will cause a spacial elongation of that orbital, which again causes the orbital energy to drop lower than the other $e_g$ orbital which is not occupied. The elongation of the orbital also induces a structural distortion to the octahedra. Figure 3.5 visualizes the effect. Simplified, the elongation causes a higher fraction of the orbital to be further away from the oxygen anion. This splitting effect also happens for unequally filled $t_{2g}$ orbitals, but to a less degree than the $e_g$ [27]. The splitting in energy levels due to Jahn Teller distortions is also included in figure 3.4.

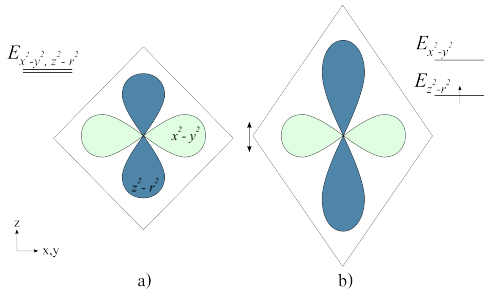


**Figure 3.5:** Schematic of the Jahn Teller effect for $e_g$ orbitals. a) Similar orbital spatial extensions when $x^2 - y^2$ and $z^2 - r^2$ are equally filled. b) Filling of only the $z^2 - r^2$ orbital lead to relative increase in extension and decrease in energy due to electrostatic repulsions.

## 3.2 $La_{1-x}Sr_xMnO_3$

$La_{1-x}Sr_xMnO_3$ (LSMO) is the Sr-doped manganite $LaMnO_3$, which had its magnetic and electronic properties charted for the first time in the mid-late 90's [28, 30], and has since been studied intensively for varying values of x [27]. Through this range of doping, the compound exhibits a variety of phases with electronic and magnetic properties that are all strongly coupled, which makes it especially interesting for applications. The phase diagram and electronic properties are shown in figure 3.6.

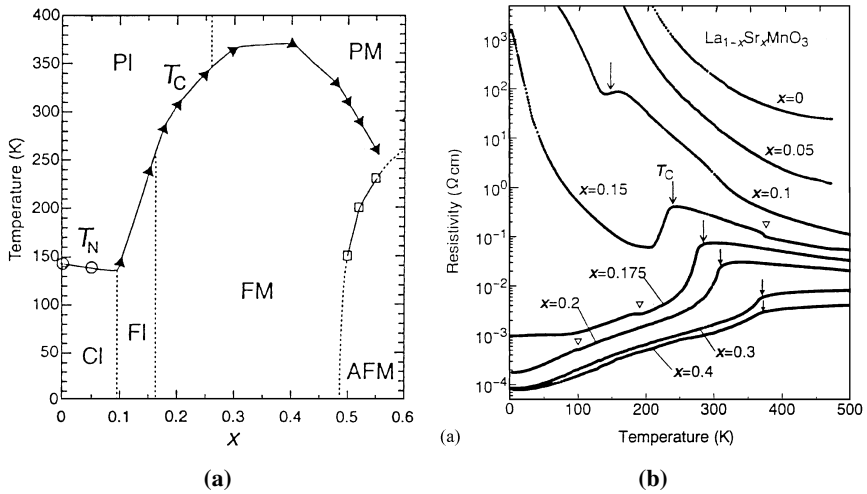


**Figure 3.6:** LSMO Properties: a) Sr-doping phase diagram showing the different phases P:paramagnetic, F:ferromagnetic, AF:antiferromagnetic, C:spin cantered, M:metal, I:insulator b) Electronic resistivity vs. Temperature for different doping values. Reproduced from [27]

Both the charge transportation and magnetic ordering phenomena are dependent on the orbital's spacial extent and orientation because it is through orbital overlap interactions can occur. The full electron configuration for LSMO is $La^{3+}_{1-x}Sr^{2+}_{x}Mn^{3+}_{1-x}Mn^{4+}_{x}O_3$, and the interesting atoms for such interactions are the $Mn^{3+}$ and $Mn^{4+}$ ions, which have electrons distributed in orbitals that overlap with the $O^{2-}$ orbitals. The overlap is dependent on the degree of tilting of the octahedra. Starting out in the far left of figure 3.6a, the manganite $LaMnO_3$ (x $= 0$) is an orthorombic perovskite where the $MnO_6$ octahedra undergo relatively high distortion rotations, as seen in figure 3.2. In $LaMnO_3$ the tilting is so extensive that it is an antiferromagnetic insulator - the overlap is too less for electron hopping to occur sufficiently, and the antiferromagnetic phenomena can be described by the superexchange mechanism - which will be explained later. Increased Sr doping values induce a change in the crystal structure, where the $MnO_6$ octahedra are "straightened" up. This can be explained by the ionic radii difference of the A-site atoms which are gradually changed as Sr substitute La. In principle, doping with Sr increases the effective average A-site ionic radii $r_A$, which induces more pressure from these ions. At $x \simeq 0.1$, the material becomes ferromagnetic, but is still an insulator. At $x \geq 0.175$, the crystal changes from

orthorombic to rhombohedral, and a half metallic and ferromagnetic phases coexist with a relatively large Curie temperature [28]. At this point, the band bending is sufficiently low to give a good orbital overlap [31], which allows both charge transfer and ferromagnetic spin ordering between the atoms, described by the double exchange mechanism.

### 3.2.1 $La_{0.7}Sr_{0.3}MnO_3$

At $x = 0.3$, LSMO is ferromagnetic and half metallic with a $T_C$ of $370\,\mathrm{K}$, close to its maximum value. The tolerance factor at $x = 0.3$ is $0.93$ and the Mn-O-Mn bonds have a bending of $166.3°$ [3]. Both the conductivity and ferromagnetic ordering in LSMO can be explained by the double exchange interaction between the Mn $3d$ and O $2p$ orbitals [28]. The double exchange interaction has been covered in previous work [1]. Its pseudocubic lattice parameters are $a = 0.388$ nm and $\alpha = 90.35\,\mathrm{deg}$. The material exhibits a $100\,\%$ spin polarization [10], i.e. all electrons in the $3d$ conduction band are parallel aligned. This can be seen for the states around the fermi level in figure 3.7, where the density of states (DOS), calculated by density functional theory (DFT) are plotted [32]. The figure shows how only spin down states from the Mn $3d$ band are available around the fermi level. The O $2p$ band is located about $1.5\,\mathrm{eV}$ below the fermi level. This can be seen to the right in the figure as an onset of spin down states.

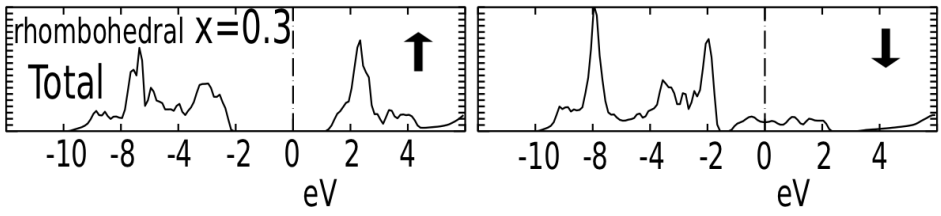


**Figure 3.7:** LSMO total density of states for $x = 0.25$, showing spin up states (left) and spin down (right). Reproduced from [32]

### 3.2.2 Bulk magnetic anisotropy

Many ferromagnetic materials express anisotropic properties - that they respond differently depending on orientation. The ease of magnetization in LSMO is dependant related to its rhombohedral structure, which yields a magnetic *easy axis* for bulk LSMO along $\langle 1\,1\,1 \rangle$ axes [33]. There are four equal $\langle 1\,1\,1 \rangle$ easy axes in a pseudo-cubic lattice, shown in figure 3.8.

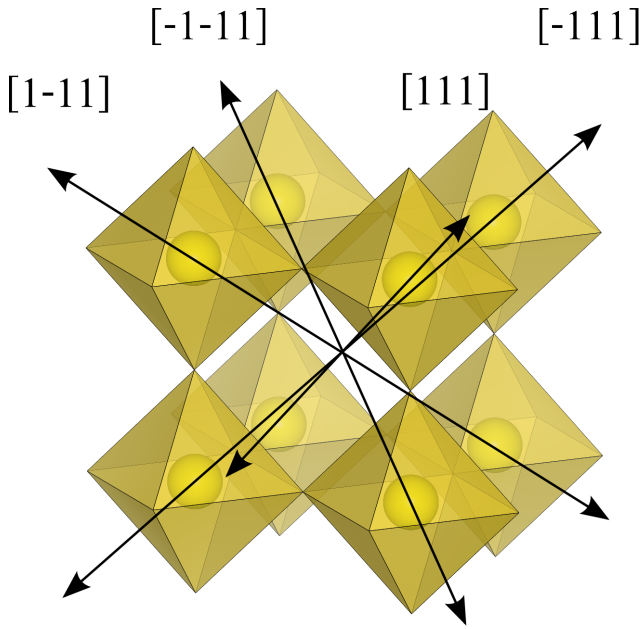


**Figure 3.8:** LSMO bulk magnetic easy axes along the [111] directions.

## 3.3 $LaFeO_3$

LFO is an antiferromagnetic and insulating perovskite with orthorombic crystalstructure. Its lattice parameters are $a = 0.5557$ nm, $b = 0.5565$ nm and $c = 0.7854$ nm. Its pseudo-cubic lattice parameters make it well fit for epitaxial growth on STO [12]. The $Fe^{3+}$ ions are $t_{2g}^3\ e_g^2$ HS [34], which means it is in a high spin state. The individual moments of each $Fe^{3+}$ ion in LFO has been found to be $4.6 \pm 0.2\mu_B$ [35]. As a solid however, due to the directions and extensions of orbitals the Fe ions are subjected to the superexchange effect [36], which causes antiferromagnetic ordering. This effect is dominant up to the material's Neel temperature ($T_N$) at $740K$, where the electron spins disorder and the material become paramagnetic. The superexchange effect is covered in previous work [1].

The electron density of states is shown in figure 3.9. The charge transfer band gap of $2.2\,\mathrm{eV}$ [37] is made up by filled oxygen $2p$ states and unoccupied upper $3d$ states, as indicated to the right in the figure.

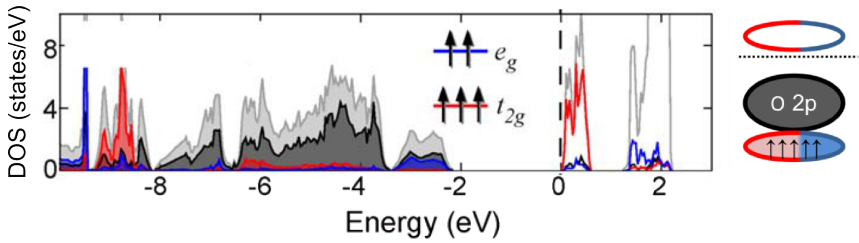


**Figure 3.9:** Density of states in bulk $LaFeO_3$. Total states are marked in grey, O $2p$ in black, Fe $t_{2g}$ in red and $e_g$ in blue. The energy scale is relative to the fermi level. Reproduced from [38].

From a pseudo-cubic perspective, bulk LFO has so-called *G-type* antiferromagnetic ordering [14], which means that the individual magnetic ions in the crystal give antiferromagnetic order in all $\langle 0\,0\,1 \rangle$ directions. An effect of this is that the (111) planes have ferromagnetic order, but with alternating spins for each plane (i.e. antiferromagnetic order in the $\langle 1\,1\,1 \rangle$ directions) as seen in figure 2.10.

## 3.4 $SrTiO_3$

$SrTiO_3$ is a diamagnetic insulator with a cubic perovskite structure, having a lattice parameter $a$ of $0.3905\,\mathrm{nm}$ [39]. It's conductivity can be adjusted through Nb-doping, where Nb substitutes Ti. A conducting substrate is suitable for doing certain magnetic measurements such as X-ray magnetic microscopy, where an insulating sample would get accumulation of charge and distort the images. While pure $SrTiO_3$ has conductivity at room temperature of $1.5 \times 10^{-1}\,\mathrm{S/cm}$ [39], a doping of $0.05\,\mathrm{wt\%}$ gives $10\,\mathrm{S/cm}$ [40].

Even though $SrTiO_3$ is diamagnetic, Liu et al. [40] has reported induced ferromagnetic phase in Nb:STO which was suggested to be in correlation with oxygen vacancies. The ferromagnetic response was reported to be strongest for Nb-doping levels of $0.5$ wt%, but also present for $0.05$ wt%. Vacuum annealing was shown to induce the phase, and annealing in air was shown to remove it. The values for the magnetic moment reported varies with annealing process, but are found to be up to $4 \cdot 10^{-4}$ emu/cc for $0.5$ wt% Nb:STO. The average coercive fields values are reported to be $300 - 400$ Oe. Figure 3.10 shows the reported hysteresis behaviour.

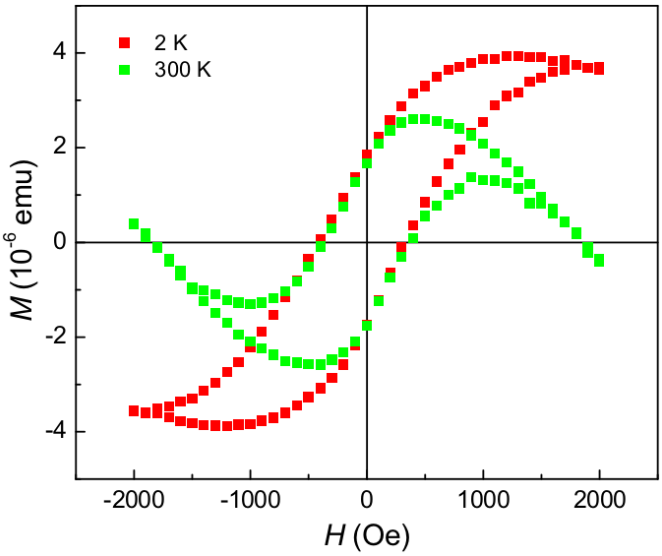


**Figure 3.10:** Hystereses and ferromagnetic behaviour reported in $0.5$ wt% Nb-doped STO. Reproduced from [40].

## 3.5 Epitaxial layers of $La_{1-x}Sr_xMnO_3$ and $LaFeO_3$

*Epitaxially grown thin films of LSMO and LFO exhibit altered properties from the bulk state. This section reviews some central important changes to magnetic properties which are found in thin films, such as for instance anisotropy or volume magnetization reduction. Reported findings in (001) and (110)-oriented epitaxial thin films are presented, and though there are few reports for the (111)-orientation, some expected effects are discussed.*

### 3.5.1 Magnetic anisotropy and magnetostriction in LSMO / STO systems

#### (001) oriented thin films

The bulk four-axis anisotropy in LSMO does not hold at surfaces, or for thin films. LSMO has had intensive study in (001)-oriented epitaxial thin films, and the magnetization directions have been shown to fall down into the (001)-plane at the surface, as seen in figure 3.11a. This has been observed both in LSMO single crystals by surface specific measurements [33] and for epitaxially grown films [41]. Generally, the magnetic anisotropy in (001) oriented LSMO thin films show a biaxial symmetry, with easy axes along [110] directions and hard axes along [001] directions [42]. Notably, [110] are the directions in the (001) surface plane which yield the lowest angles to the [111] directions, which are the easy axes in bulk LSMO. The change of easy axis directions has therefore in single crystals been explained by moments close to the surface lowering their out-of-plane (or out-of-surface) magnetization component by rotating the moments into the surface plane [33]. This explanation could hold for thin films as well, but in their case the strain imposed by the underlying substrate has also been reported to be of great importance, and may dominate the easy axis directions in thin films [43, 44]. Another factor which also may cause magnetic anisotropy in thin films is the presence of step edges in the substrate [45]. By having substrates with small miscut angles from low index planes, one obtains step-edged surfaces, as shown in figure 3.11b. These edges can introduce a new uniaxial anisotropy along the edge directions, and has been shown to permit tailoring of anisotropic properties for application purposes. The step-edge induced anisotropy has been reported to do dominate over the substrate-to-film strain anisotropy for films up to $120\,\mathrm{nm}$, which are relatively thick films [42].

For thin films of LSMO grown on (001) $SrTiO_3$, the magnetization at the interface is also significantly lowered, which becomes especially evident for thicknesses below $20\,\mathrm{nm}$. This has been been reported to be in correlation with tetragonal distortions which occur in correlation with imposed epitaxial strain from the substrate [46]. More recent investiagionts of a so-called magnetic *dead layer* have suggested a link between loss of magnetization and presence of oxygen vacancies [42]. Dead layer thicknesses of down to 4 uc (unit cells) have been achieved [47]. Investigation of charge transfer has also been done for (001) LSMO / $SrTiO_3$ interfaces to check whether loss magnetism is coupled to electrons transferring across the interface due to unequal valence of the B cations in the two materials, however results are conflicting. Superlattices of LSMO / $SrTiO_3$ have both indicated robust valence states and no charge transfer [48], but also transfer and induced magnetism in diamagnetic $SrTiO_3$ [49].

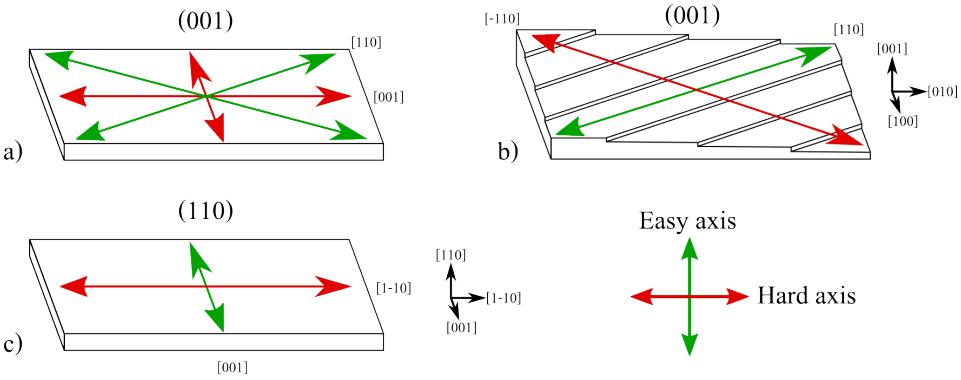


**Figure 3.11:** Easy axes in epitaxial LSMO thin films. a) (001)-oriented film on flat substrate. b) (001)-oriented film on substrate with miscut angle. c) (110)-oriented film on flat substrate.

### (110) oriented thin films

Studies have also been done for (110)-oriented films. Since the bulk easy axes in [111] directions are lying in (110) planes, the observed easy axes on these epitaxial films could be expected to still be in [111] directions in correspondence with the previous explanation of lowering out-of-plane magnetic components. However here the substrate strain seems to dominate. For LSMO films grown on (110) $SrTiO_3$ substrates, the easy axis has been reported to fall along [001] directions, while [110] directions show to be hard axes [43,50]. This is believed to be due to magnetostriction which occurs due to an anisotropy of tensile strain from the substrate [51], which demonstrates the importance of how anisotropic strain may influence magnetic anisotropy in oxide thin films. The magnetic moment is though not reported to be suppressed in the same extent as in the (001) orientation, and this is due to the different nature of crystal distortion, being monoclinic in (110) but tetragonal in (001) [46]. Hence epitaxial strain influences both magnetic anisotropy and magnetization, but in different ways.

### Hexagonal symmetry and the (111) orientation

While the (001) and (110)-orientations of LSMO thin films have had extensive study, little has been done in the (111)-orientation. Epitaxial films of LSMO on (111) $SrTiO_3$ are subjected to tensile stress resulting in trigonal distortion [46]. However the biaxial Young's modulus is isotropic in the (111) plane, which suggest that the magnetization should fall into the plane and be governed by magnetocrystalline effects rather than magnetostriction [52]. Since the (111) plane has hexagonal crystal symmetry, shown in figure'3.12, the magnetic properties are expected to be different than in the (001) and (110)-orientations.

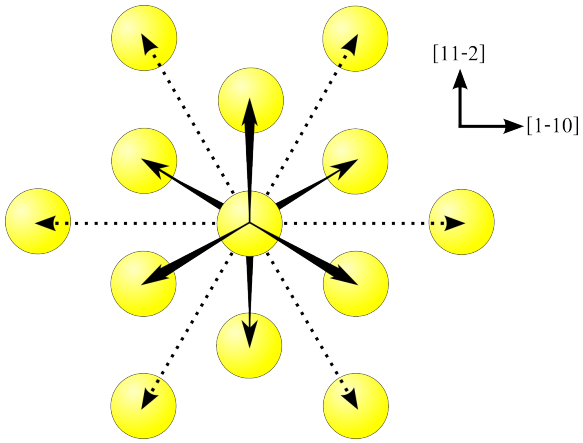


**Figure 3.12:** Hexagonal symmetry in the distribution of magnetic Mn cations in the 111 plane of LSMO. Dotted lines point towards the nearest Mn atoms which are in the same (111)-plane as the central Mn atom. Continuous lines point towards the nearest Mn atoms in the (111)-plane above and below the central Mn atom.

Recent investigations of magnetization directions during $180\,\mathrm{degree}$ swithing on (111) oriented thin films of LSMO on $0.05\%$ Nb-doped $SrTiO_3$ have revealed a 6 fold magnetic anisotropy, correlating well with the crystalline symmetry of the (111) plane. In addition the macroscopic behaviour is isotropic, i.e. values of the coercive fields and saturation magnetizations are independent on field directions [52]. In addition values of coercive fields are lower than reported for (001) oriented films, indicating freely moving domain walls.

## 3.5.2 Heterostructures

### Spin coupling

As mentioned, antiferromagnets may alter the properties of ferromagnets when put adjacent to each other, such as causing an exchange bias or changing the coercive field [53]. An important feature of ferromagnet / antiferromagnet junctions is how their spin moments align relative to each other. For the (001) orientation, if the spin in the ferromagnet aligns in a *collinear* fashion (i.e. spins aligned along the same axis), one way or the opposite -

the state would be the same since in both cases there an equal amount of ferromagnetic and antiferromagnetic couplings due to alternating spins in the interface layer of the antiferromagnet. A collinear ordering is shown in figure 3.13a. In (001) oriented systems of LFO / LSMO, so called *spin-flop* interaction has instead been reported consistently by various techniques [54]. In this situation, the ferromagnet has perpendicular oriented spins relative to the antiferromagnet, as illutrated in figure 3.13b).

Figure 3.13c, d and e illustrates possible orientations. For a spin compensated surface such as in the (001) and (110) orienataions, an increase in coercivity is predicted, but no exchange bias [55]. However in the (111) orientation there may be a stronger exchange interaction which can cause both exchange bias or increased coercivity.

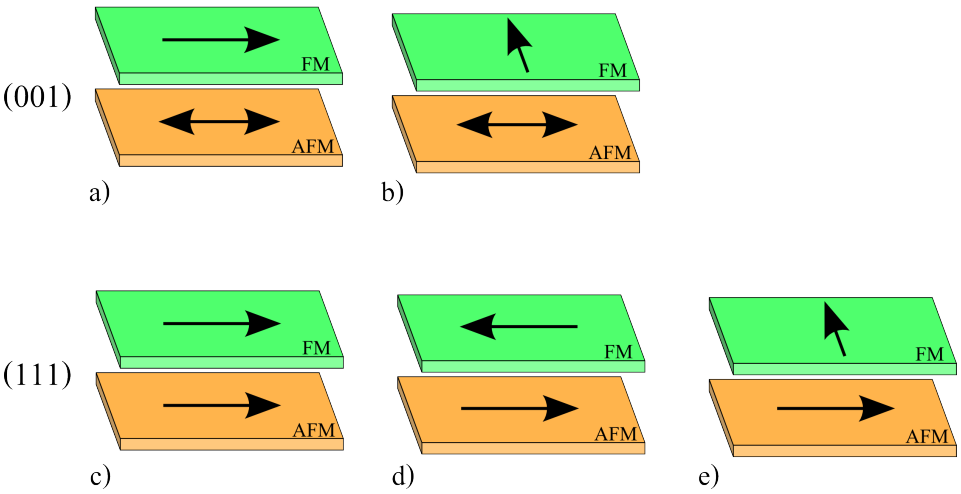


**Figure 3.13:** Possible spin orientations at the LSMO / LFO interface. a) Collinear ferromagnetic interaction, b) collinear antiferromagnetic interaction, c) Spin flop interaction

### Exchange bias

Some material systems show so-called *exchange bias*. This is easily observed in hysteresis measurements by the loop being shifted along the H-field axis by an amount often labeled $H_E$. This phenomenon is well known for occuring in ferromagnetic / antiferromagnetic bilayers, where the interaction between the two materials causes a preferred spin direction for the ferromagnet, but it has also been observed in systems with non-antiferromagnetic materials. Exchange bias effect has been reported in (001) LSMO / STO multilayer systems, when the samples have been field cooled [56]. The behaviour is shown in figure 3.14. The value of the exchange bias field showed exponential decay with increased temperature. Since STO is diamagnetic and therefore not expected to yield an exchange bias effect, it was proposed to originate from disordered spin states in the LSMO layer close to the interface, which was caused by epitaxial strain from STO. Other investigations have shown a correlation of the exchange bias effect with reduced oxygen pressures during film growth procedures, and therefore oxygen vacancies have been proposed to induce an antiferromagnetic layer in LSMO near STO and cause the effect [57].

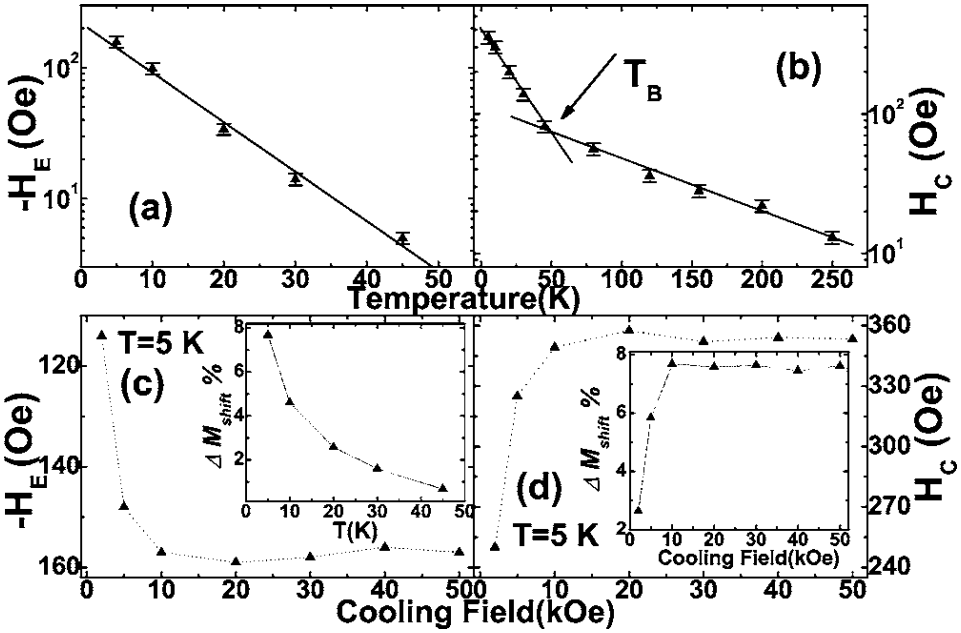


**Figure 3.14:** Reported exchange bias effect in (001)-oriented multilayers of LSMO and STO. a) shows the exchange bias values of temperatures below 50 K. b) shows the coercive field values from the corresponding measurements. c) shows the variation of exchange bias as function of magnetization field, and d) shows the corresponding coercive field values. Reproduced from [56].

# 4. Experimental

*In this chapter, the experimental process is described. First a description of the sample preparations, then followed by an overview of all samples, and lastly the process of the magnetic measurements done with the vibrating sample magnetometer (VSM). Theory on the VSM has been covered in previous work [1].*

## 4.1 Sample preparation

*Samples where grown by pulsed laser deposition (PLD) by Ingrid Hallsteinsen, according to published works [13].*

### 4.1.1 Preparation of samples for VSM measurements

In order for the samples to fit the VSM sample holders, they needed to be cut to dimensions less than $5 \times 5$ mm. This was done by using a diamond cutter, and subsequent rinse with ethanol. In order to scale measured magnetic moments to the volume of the samples, their surface area was estimated by imaging while the samples placed on a mm-sheet paper, and analysing the dimensions with ImageJ [58]. An overview of the samples is shown in figures 4.1, 4.2 and 4.3, and estimated values are summarized in table 4.1. As seen from the sample pictures, some samples may seem to have parts of material outside the yellow marking lines. The area outside consists of either shadows, or substrate material (i.e. no epitaxial layers) and are there due to imperfect cutting. The yellow marking lines are ensured to only surround the actual surface area of the epitaxially grown layers.

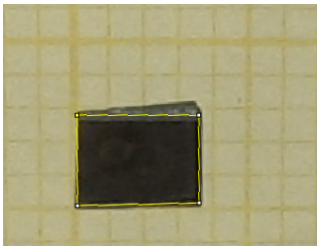

**(a)** LSMO (2.3 nm) / Nb:STO

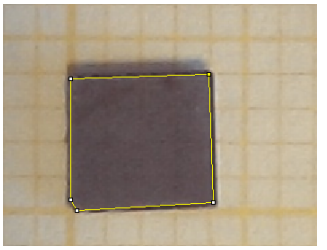

**(b)** LSMO (4 nm) / Nb:STO

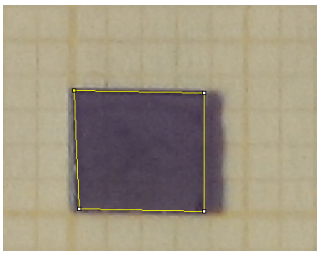

**(c)** LSMO (7 nm) / Nb:STO

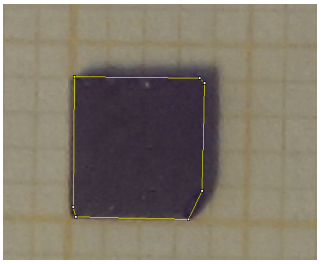

**(d)** LSMO (21 nm) / Nb:STO

**Figure 4.1:** LSMO / Nb:STO film samples imaged on mm-sheet paper. The thin yellow lines on the paper indicate 1 mm distances. Yellow lines on the samples indicate how surface area was estimated.

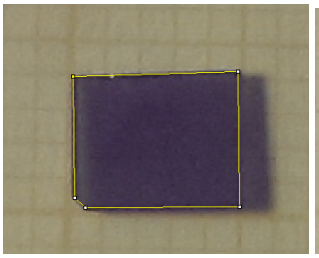

**(a)** LFO (4 nm) / LSMO (4 nm) / Nb:STO

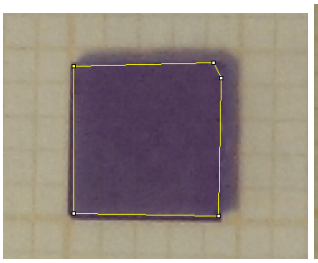

**(b)** LFO (4 nm) / LSMO (7 nm) / Nb:STO

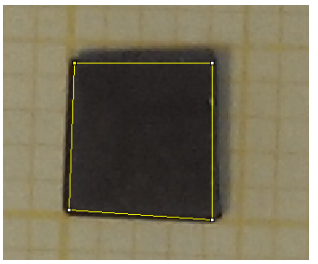

**(c)** LFO (4 nm) / LSMO (21 nm) / Nb:STO

**Figure 4.2:** LFO / LSMO / Nb:STO bilayer samples imaged on mm-sheet paper. The brown lines on the paper indicate 1 mm distances. Yellow lines on the samples indicate how surface area was estimated.

**(a)** LSMO (4 nm) / LFO (2 nm) / STO

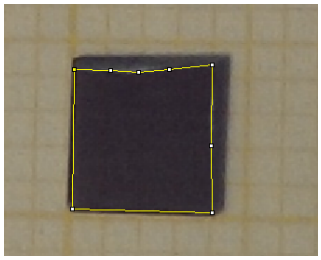

**(b)** LSMO (4 nm) / LFO (4 nm) / Nb:STO

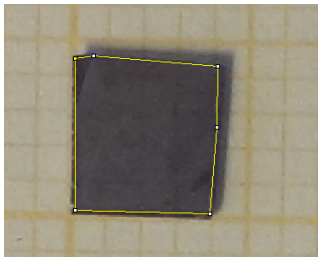

**(c)** LSMO (4 nm) / LFO (7 nm) / Nb:STO

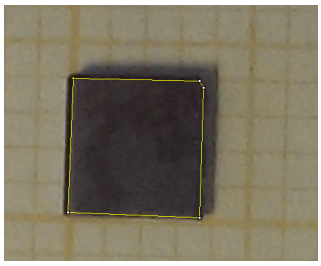

**(d)** LSMO (4 nm) / LFO (21 nm) / Nb:STO

**Figure 4.3:** LSMO / LFO / Nb:STO bilayer samples imaged on mm-sheet paper. The thin yellow lines on the paper indicate 1 mm distances. Yellow lines on the samples indicate how surface area was estimated.

**Table 4.1:** Estimated values from the samples. The thickness column corresponds to the layer which has varying thickness for that configuration.

| Layer configuration | thickness ($d$) (nm) | Area (cm$^2$) | LSMO volume (cm$^3$) | Mn atoms |
|---|---|---|---|---|
| | 2.3 | 0.086 | $1.98 \cdot 10^{-8}$ | $3.4 \cdot 10^{14}$ |
| LSMO ($d$) / | 4 | 0.152 | $6.09 \cdot 10^{-8}$ | $1.04 \cdot 10^{15}$ |
| Nb:STO | 7 | 0.124 | $8.69 \cdot 10^{-8}$ | $1.49 \cdot 10^{15}$ |
| | 21 | 0.142 | $2.99 \cdot 10^{-7}$ | $5.11 \cdot 10^{15}$ |
| LFO (4nm) / | 4 | 0.187 | $7.47 \cdot 10^{-8}$ | $1.28 \cdot 10^{15}$ |
| LSMO ($d$) / | 7 | 0.191 | $1.33 \cdot 10^{-7}$ | $2.29 \cdot 10^{15}$ |
| Nb:STO | 21 | 0.141 | $2.97 \cdot 10^{-7}$ | $5.08 \cdot 10^{15}$ |
| | 2 | 0.102 | $4.10 \cdot 10^{-8}$ | $7.01 \cdot 10^{14}$ |
| LSMO (4 nm) / | 4 | 0.155 | $6.22 \cdot 10^{-8}$ | $1.06 \cdot 10^{15}$ |
| LFO ($d$) / | 7 | 0.171 | $6.84 \cdot 10^{-8}$ | $1.17 \cdot 10^{15}$ |
| Nb:STO | 21 | 0.141 | $5.66 \cdot 10^{-8}$ | $9.68 \cdot 10^{14}$ |

## 4.2 VSM measurements

### 4.2.1 Calibration measurements

Control measurements without sample holders and with empty sample holders were conducted in order to determine the precision of the magnetic measurements. Without any sample holder inserted into the VSM, only noise was obtained with magnitude in the order of the VSM's listed resolution limit($10^{-6}$ emu) [59], shown in figure 4.4a. With an empty sample holder, a magnetic signal was found, shown in figure 4.4b. The magnitude of this signal was also in the range of the VSM's resolution limit, and is thus presumed to be expected behaviour. Care was therefore taken when interpreting subsequent measurements done to the samples, especially when the sample signals were in the order of the resolution limit.

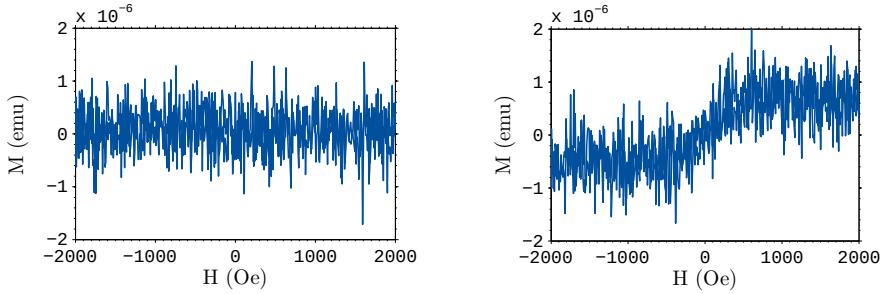


**Figure 4.4:** VSM calibration measurements done with 2000 Oe fields at room teperature. a) Without any sample holder inserted. b) With a sample holder inserted.

### 4.2.2 Magnetic measurement procedures

The samples were mounted onto quartz sample holders by using a gum resin (GE Varnish). The samples where then inserted into the VSM chamber, followed by chamber purging and sealing with He. Magnetic measurements were conducted at various temperatures in the range 50-400 K, under a He pressure varying in the range of 35-70 Torr.

All the samples were mounted so that the magnetic field was aligned parallel to the sample surface, and along the $[1\,\bar{1}\,0]$ direction.

## 4.3 Processing results

When processing the measurement data, most of the samples showed a ferromagnetic phase above the curie temperature of LSMO. While the moment is easily observable above $T_C$, it is likely also present at lower temperatures. In order to compare the magnetic behaviour of the LSMO films at low temperatures, the moment measured from the additional phase has been subtracted from the measurement data. This was done by subtracting the moment measured at $T_C$ as mentioned, making the data show an exact zero moment at this

temperature. The subtraction is indicated in figure 4.5. While assuming that the moment from the additional magnetic phase does not change significantly with temperature under $T_C$, interpretation of the difference in the ferromagnetic LSMO layer responses was done. It is noted however that the values far from $T_C$ could be inaccurate, as the moment from the additional phase could vary with temperature. This was equally done for all the samples, and all reported values of moment have been adjusted in this manner. In the result chapter, the figures showing moment curves have been adjusted, and the raw data is shown in figure insets.

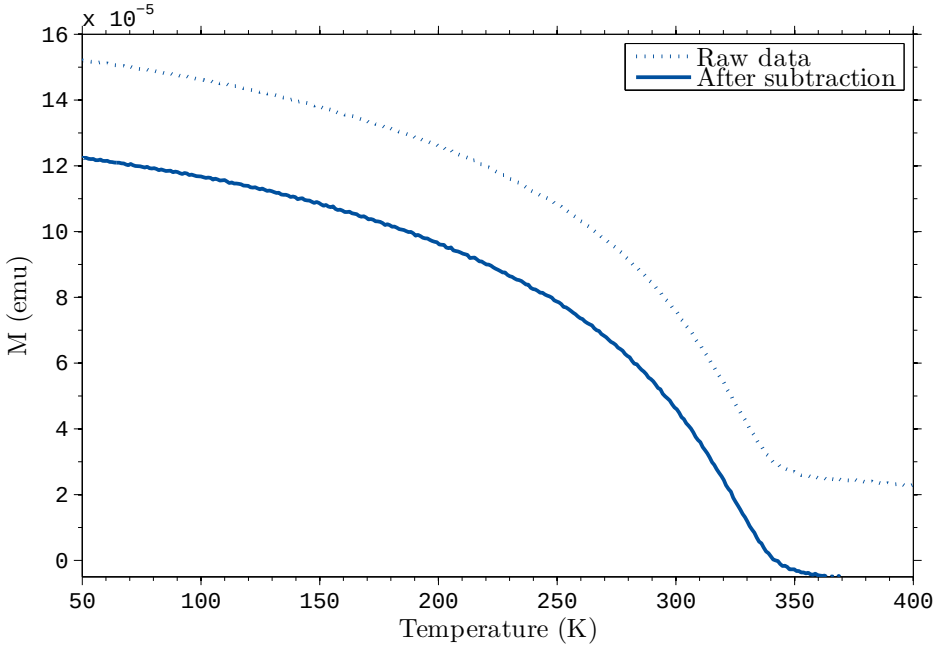


**Figure 4.5:** Example of a moment versus temperature graph, and how values from the ferromagnetic phase above Tc is subtracted.

The curie temperature was estimated from moment versus temperature graphs, by estimating the intersection point of the two tangents of the curve, which bounds the curie temperature. An example of the estimation is shown in figure 4.6

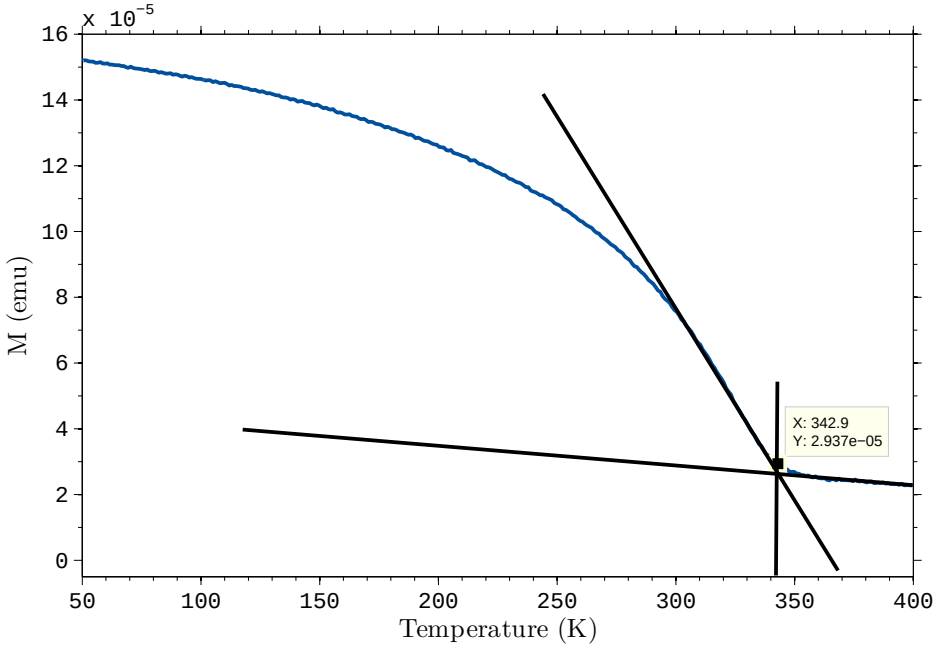


**Figure 4.6:** Example of the estimation of curie temperature from a moment versus temperature graph.

# 5. Results and Discussion

*In this chapter, the experimental results will be presented and discussed in a structural order. First the LSMO thin films are presented, followed by the bilayer system with a 4 nm LFO top layer, and finally the bilayer system with underlying LFO layer. For each individual system, observed magnetic moments, hysteresis behaviour, coercive fields and exchange bias are discussed, and compared with the other systems.*

## 5.1 (111) LSMO / Nb:STO

*The measurement results from the (111) LSMO / Nb:STO samples will primarily be compared with reported finding on (001) and (110) oriented LSMO / Nb:STO systems.*

### 5.1.1 Magnetic moment

Figure 5.1 shows the measured temperature behaviour of the saturation magnetization in LSMO / Nb:STO thin films, where the moment has been scaled to the number of Mn atoms in the samples and the moment has been normalized to be zero at $T_C$. The figure inset shows the raw data with moment in emu.

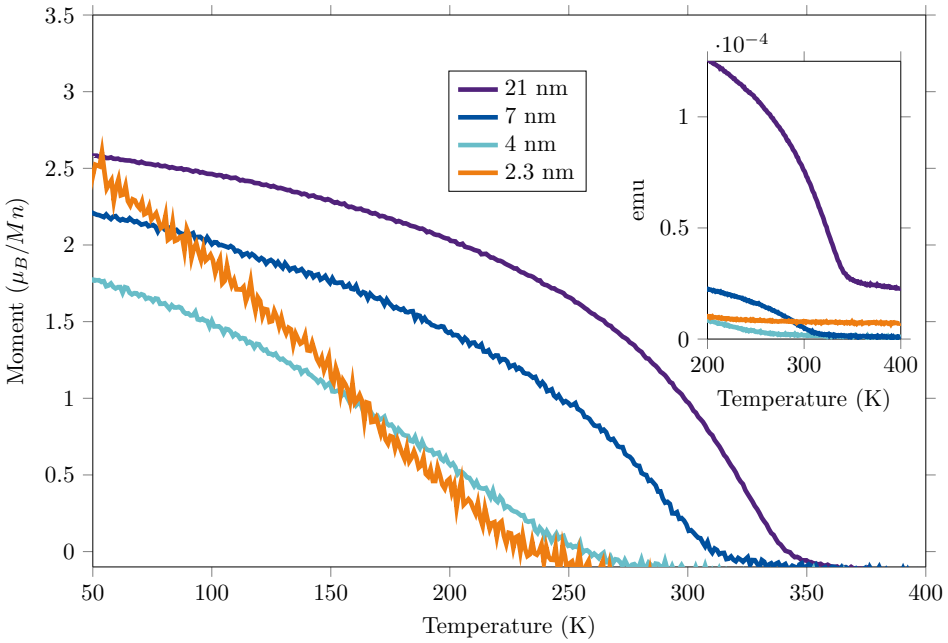


**Figure 5.1:** LSMO / Nb:STO Moment versus temperature, measured at $H = 2000\,\mathrm{Oe}$ after 20kOe field cooling from 400 K. All measured data has had the value at $T_C$ subtracted for all temperatures. The inset shows the raw data before subtraction.

The magnetic moment from all the samples is found to be highest at 50 K, and decay as temperature increases. For the thickest film, with 21 nm LSMO layer, the curve shape resembles typical behaviour reported on (001) LSMO / STO systems. The measured moment at 50 K is $2.6\,\mu_B/\mathrm{Mn}$ (502 emu/cc). This is lower than the bulk values of $3.7\,\mu_B/\mathrm{Mn}$ (600 emu/cc) [46,47], however the magnetization may be higher at temperatures below 50 K. It may also be an indication that 21 nm is not a sufficient thickness for (111) LSMO / Nb:STO for it to exhibit bulk ferromagnetic properties. The films are known to be fully epitaxially strained, i.e. the strain from the substrate is carried through the whole film [52]. A reduction of moment could for instance occur due to the films being subjected to tensile strain from the substrate, as strain is known to suppress ferromagnetic behaviour and lower the transition temperature in ferromagnetic thin films [11, 60, 61]. However the epitaxial strain imposed by STO in the (111)-orientation is similar as in (001) [46], thus there is no clear indication that strain will impact volume magnetization more in the (111)-orientation.

A further reduction in moment is also observed for the films thinner than 21 nm. Fig-

ure 5.2 shows the saturation magnetization at 50 K from the films plotted against thickness (inverse). The 2.1 nm sample shows deviation from the trend of reduced moment as thickness decreases, as it has a higher moment at 50 K than both the 4 and 7 nm film samples. The behaviour of moment in this film is deviating to such extent it is suggested to be further examined before drawing any more conclusions. The value from this sample is therefore excluded from the linear estimation in figure 5.2. The other samples show a trend of decreasing moment with decreasing thickness.

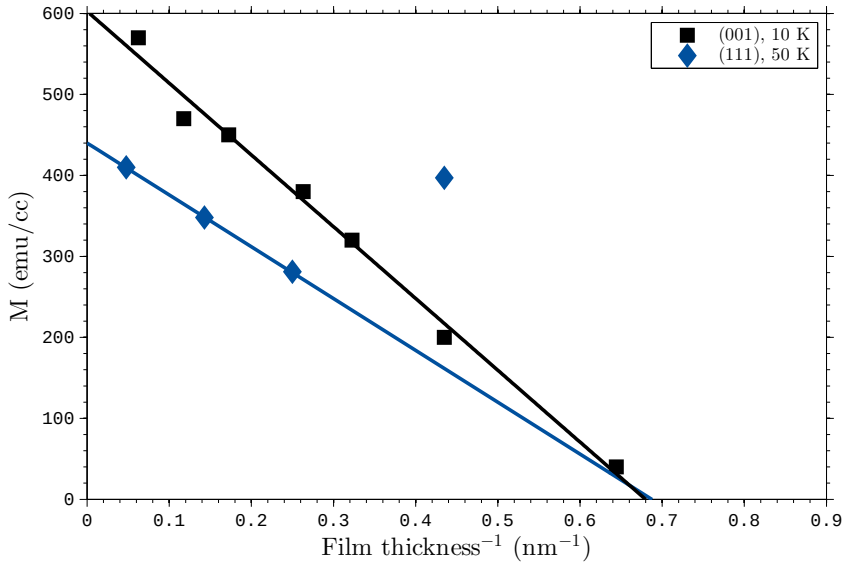


**Figure 5.2:** Saturation moments measured at 50 K with a linearization projecting the dead layer thickness. (001) data is reproduced from Monsen et al. [47]

Another possible reason for reduced moment is that a magnetic and electric dead layer may be formed at the interface. From figure 5.2, the presence of a dead layer is indicated and estimated by linear regression to be roughly $1.5\,\mathrm{nm}$, in correlation with a volume magnetization of $2.8\,\mu_B/\mathrm{Mn}$ (440 emu/cc). The volume magnetization is lower, but the dead layer thickness is similar to what is reported in (001)-oriented LSMO / Nb:STO, where the same estimation method has been applied and given a volume magnetization of $3.7\,\mu_B/\mathrm{Mn}$ and dead layer thickness of $1.6\,\mathrm{nm}$ [47]. The (001) reported data is included in figure 5.2 for comparison. A suggestion is that the reduction is thickness related, which could indicate that (111) epitaxial films are more sensitive to thickness than (001) films. Since the compared data from the (001) system is obtained at a lower temperature (10 K), where the magnetic moment also may be higher for the (111) films, the moment curves from figure 5.1 were extrapolated to 10 K for better comparison. However the difference in dead layer thickness estimation was negligible, and it is thus not shown in the figure. Regarding the location of a dead layer in the film - it cannot be fully interpreted from these results alone. There could be non-magnetic layers of LSMO at the top of the film due to

for instance surface reconstructions, as well as due to the strain at the LSMO / Nb:STO interface. The $1.5\,\mathrm{nm}$ dead layer is thus not necessarily all at the film to substrate interface.

The curve shapes in figure 5.1 show that the sharpness of the transition temperature also decreases with film thickness. This resembles what has been observed in 001 systems [47, 61–63], and indicate that the thinnest films have less homogeneity. This can be expected as the film consists of an interface region near the substrate, a bulk-like region in the center, and perhaps also a structural reconstructed region at the top. As the film thickness is reduced, the bulk-behaving region will decrease and the boundary regions will be more prominent.

A reduction of $T_C$ is also observed with decreasing film thickness, as seen from figure 5.1. The thickness dependency of $T_C$ is plotted in figure 5.3, which indicates a non-linear reduction in $T_C$ as the film thickness is decreased. Such non-linear reduction of $T_C$ has reported on (001)-oriented LSMO/STO systems [11, 47, 64], and reported data is included in the figure for comparison. The reduction of $T_C$ is believed, as with the reduced moment, to be in correlation with structural influence from the interface such as strain [11, 60, 61].

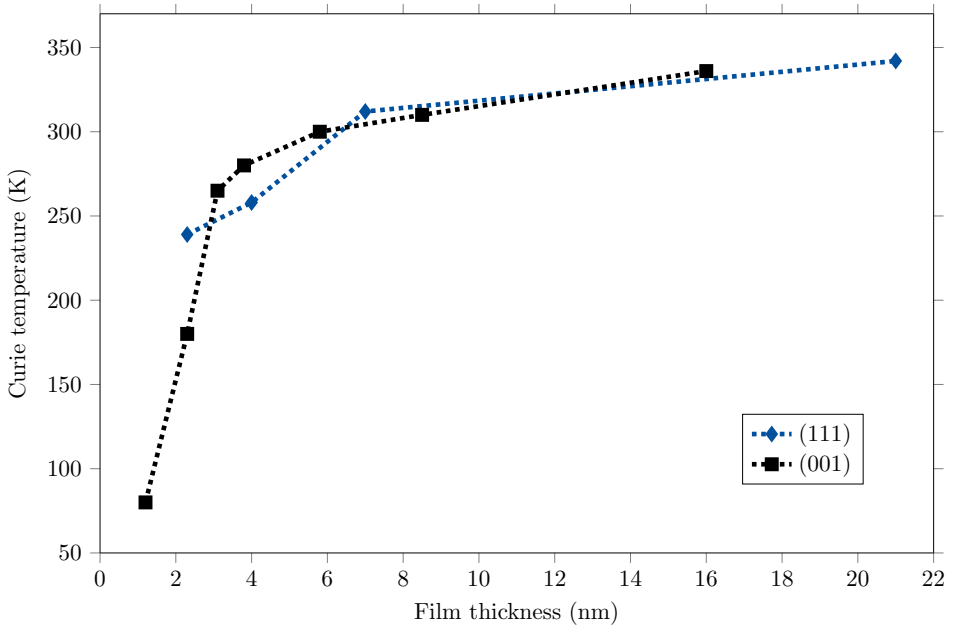


**Figure 5.3:** LSMO/Nb:STO thickness dependence of $T_C$. (001) data is reproduced from Monsen et al. [47].

**Observed magnetic phase above Tc**

All samples show a moment present above $T_C$. The magnitude of this moment is for two of the samples - with $4\,\mathrm{nm}$ and $7\,\mathrm{nm}$ LSMO layers - in the same order as the VSM's resolution limit ($\sim 10^{-6}$ emu), and is thus difficult to interpreted, but for the $21\,\mathrm{nm}$ LSMO film sample the moment above $T_C$ is about a factor of 20 higher than the resolution limit. This suggests that there is an additional magnetic phase present in the samples, which is most prominent in the $21\,\mathrm{nm}$ sample. Hysteresis measurements conducted above $T_C$ revealed what seems like a ferromagnetic phase. Upon a 2 hour annealing of the 21 nm LSMO sample at $500\,^{\circ}\mathrm{C}$ in $1\,\mathrm{atm}$ pressure of $O_2$, the magnetic moment from this phase was found to drop by 50 %. The results are shown in figure 5.4. A suggested origin of the hysteresis is an induced ferromagnetic phase in the substrate due to oxygen vacancies, which may have occurred during during growth. The reason why the observed phase is more present in one of the four samples is unknown. Since the oxygen pressure during growth is controlled, and all three films were grown with the same parameters, there are no clear variations in growth conditions that can be linked directly to this observed difference. The moment values for the different samples seen above $T_C$ are given in table 5.1.

**Table 5.1:** Measured moments in the LSMO / Nb:STO samples at $380\,\mathrm{K}$ above $T_C$, scaled to the volume of the Nb:STO substrate.

| Sample | Moment (emu/cc) |
|---|---|
| LSMO (2.3 nm) / Nb:STO | $7.1 \cdot 10^{-5}$ |
| LSMO (4 nm) / Nb:STO | $1.8 \cdot 10^{-4}$ |
| LSMO (7 nm) / Nb:STO | $2.3 \cdot 10^{-4}$ |
| LSMO (21 nm) / Nb:STO | $3.4 \cdot 10^{-3}$ |

The values are comparable to the reported value in 0.5 wt% Nb-doped (001) STO of $4 \cdot 10^{-4}$ emu/cc, however larger than what is reported for 0.05 wt% [40]. The coercive field is about $100\,\mathrm{Oe}$, which is smaller than what is reported (300-400 Oe). Though the values differ from reports on (001) Nb:STO, the (111) Nb:STO has a different surface crystallography, and there are epitaxially grown films on top. Since oxygen vacancies, which are suggested to induce the ferromagnetism, are believed to be localized at the substrate surface [40], many factors could be causing a different behaviour.

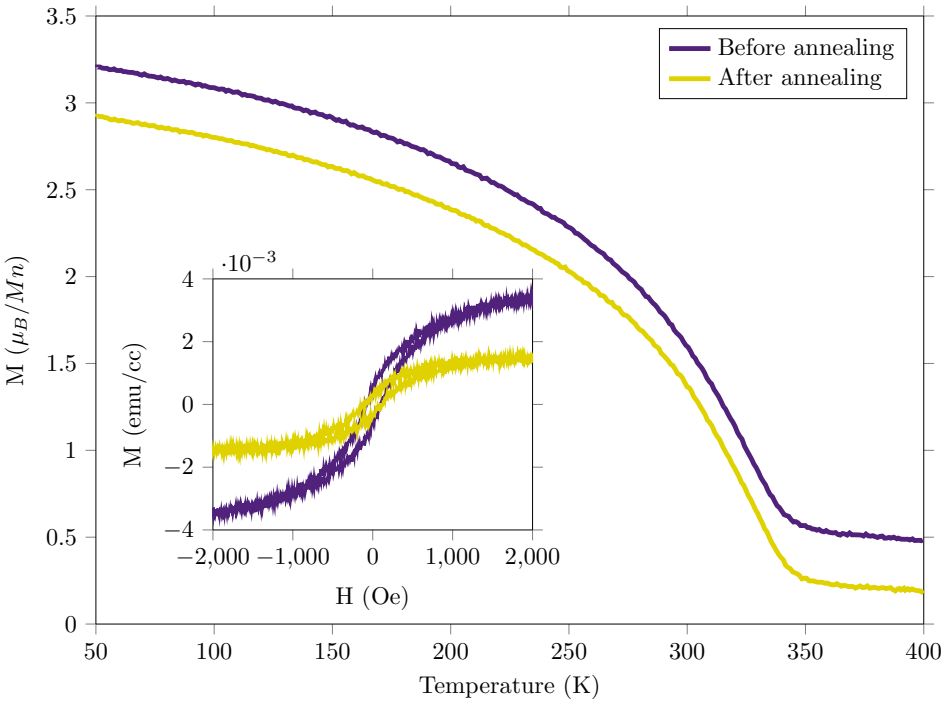


**Figure 5.4:** Change in the ferromagnetic phase observed above $T_C$ upon oxygen annealing of the 21 nm LSMO sample for 2 h in 1 atm $O_2$. The moment in the main figure is scaled to the number of Mn atoms in the LSMO layer. The figure inset shows the hystereses obtained at 375 K, and the moment is scaled to the volume of the substrate.

### 5.1.2 Coercive field

Hystereses obtained at 50 K are shown in figure 5.5. The values of the coercive fields are significantly lower than reported on (001) LSMO / STO systems. Tian et al. [65] for instance reported a value of $44$ Oe at $50$ K for an 8 uc ($\sim$ 3nm) (001) LSMO / STO film. The low coercive field indicates that the domain walls move freely without significant pinning, which could be a sign of few structural defects in the films [52]. Values of the coercive fields were obtained with 25 K intervals, and the temperature dependency is plotted in figure 5.6. The figure inset shows the dependency with normalized temperature ($T/T_C$). The highest values are obtained at 50 K, and are all lower than 20 Oe as seen from the figures.

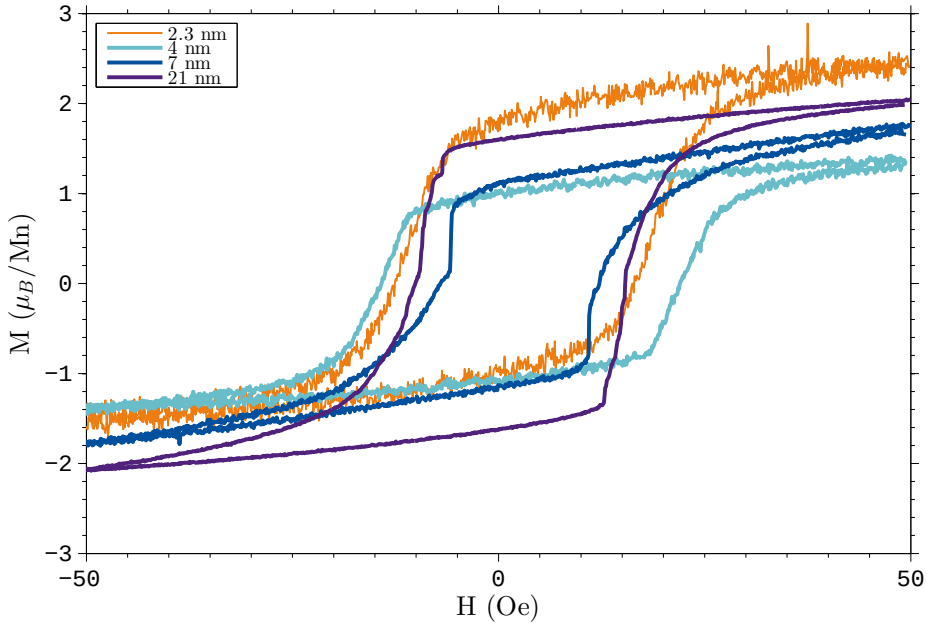


**Figure 5.5:** LSMO/Nb:STO Hystereses obtained at 50K

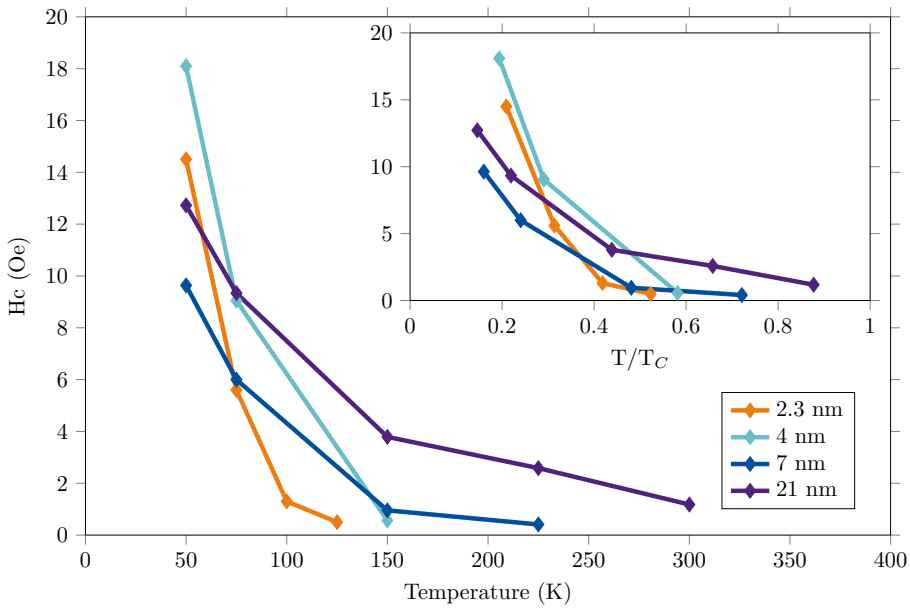


**Figure 5.6:** LSMO / Nb:STO Temperature dependency of the coercive field

A temperature dependency is seen in all samples with an increase in $H_C$ towards lower temperatures, but no obvious trend is observed relative to the thickness of the LSMO films. Studies done on the (001)-oriented system has been reported to show an increase in $H_C$ as temperature decreases [11, 66], and the effect is correlated with the temperature dependency of magnetic grains sizes. Reduced film thickness is also reported to lead to increased $H_C$ [11, 47, 61], and this effect is reported to appear for films thinner than 4 nm. However there is no significant trend from the results with respect to thickness, and the thinnest sample of 2.3 nm has a lower $H_C$ than the 4 nm sample at 50 K. The measurements from the reports cited are conducted at lower temperatures (5 or 10 K), where the effect may be more prominent than at 50 K. There might thus be such a trend with thickness for the (111)-oriented system at lower temperatures, but it cannot be observed from the presented results.

### 5.1.3 Exchange bias

All of the LSMO / Nb:STO thin films show exchange bias. This was found by magnetizing the samples in a 1 kOe field, followed by $\pm 50$ Oe field measurements which fully enclose the LSMO hysteresis loops. The magnetization measurements revealed both hysteresis shifts along the moment and field axes, as shown in figure 5.7. Since the LSMO hystereses lie shifted along the moment axis, $H_C$ and $H_E$ values cannot be simply read from the field axis. The hystereses were hence normalized to their saturation magnetizations as shown in figure 5.8, where the coercive field and exchange bias values were extracted. Values obtained from measurements with 25 K intervals revealed a temperature dependency of the exchange bias, which is shown in figure 5.9.

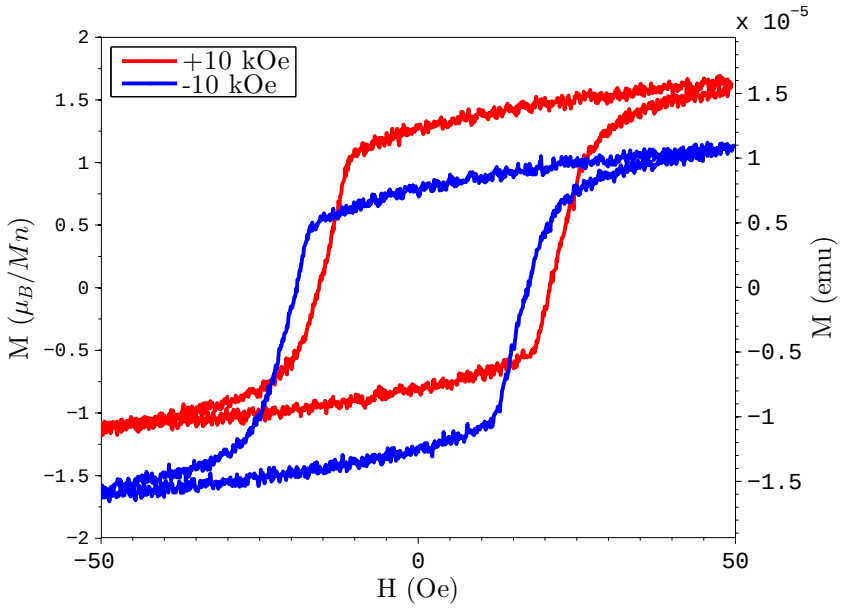


**Figure 5.7:** Hystereses obtained from LSMO/Nb:STO films after magnetizations in 10 kOe fields, showing shifts along both axes.

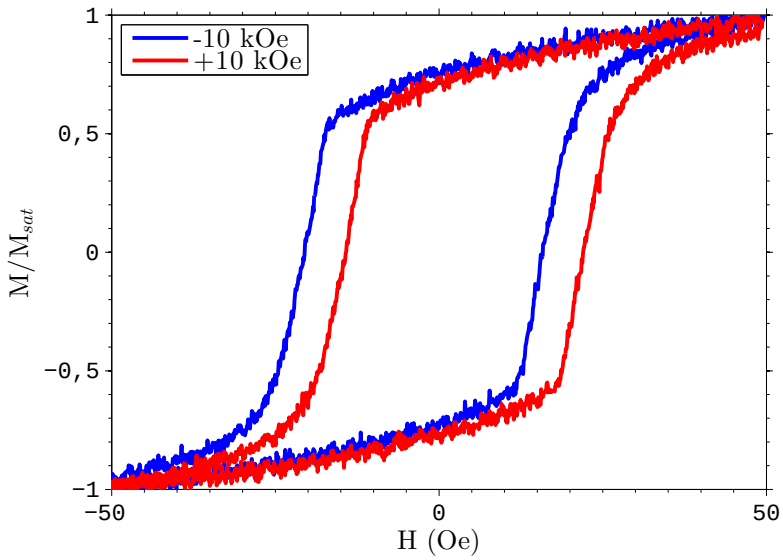


**Figure 5.8:** Hystereses normalized to saturation moments, where the values of $H_C$ and $H_E$ was extracted.

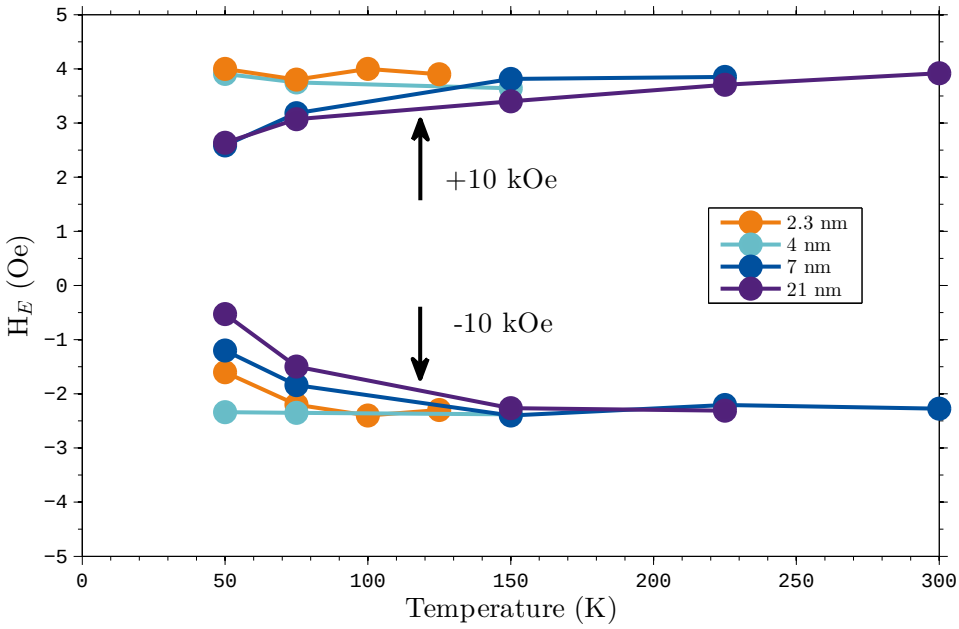


**Figure 5.9:** LSMO/Nb:STO Exchange bias after sample magnetization in a 10 kOe field at each temperature.

The exchange bias field $H_E$ found in all samples seems to converge to the same value as temperature increases, 3.5 Oe with 10 kOe and $-2.5$ Oe with $-10$ kOe. The $H_E$ field is hence found to be asymmetrical, by being consistently higher in the direction labelled as a positive field. Some of the films also show decrease in $H_E$ towards the lowest temperatures. The decrease towards the lowest temperature is less for the two thinnest film samples (2.3 and 4 nm), which could indicate that the effect is more robust in thinner films. The positive and negative magnetization fields are both oriented in the surface plane and parallel to a crystallographic $\langle 1\,\bar{1}\,0\rangle$ direction. Hence there is no crystallographic difference for the two magnetizations which can explain the asymmetry. This could indicate that the phase causing the bias may simply not be fully switched by the applied magnetization field. However magnetization fields up to 30 kOe still show an asymmetry, though the magnitude of $H_E$ is found to change with magnetization field. The magnetization field dependency for the 4 nm LSMO sample is shown for 50 K in figure 5.10.

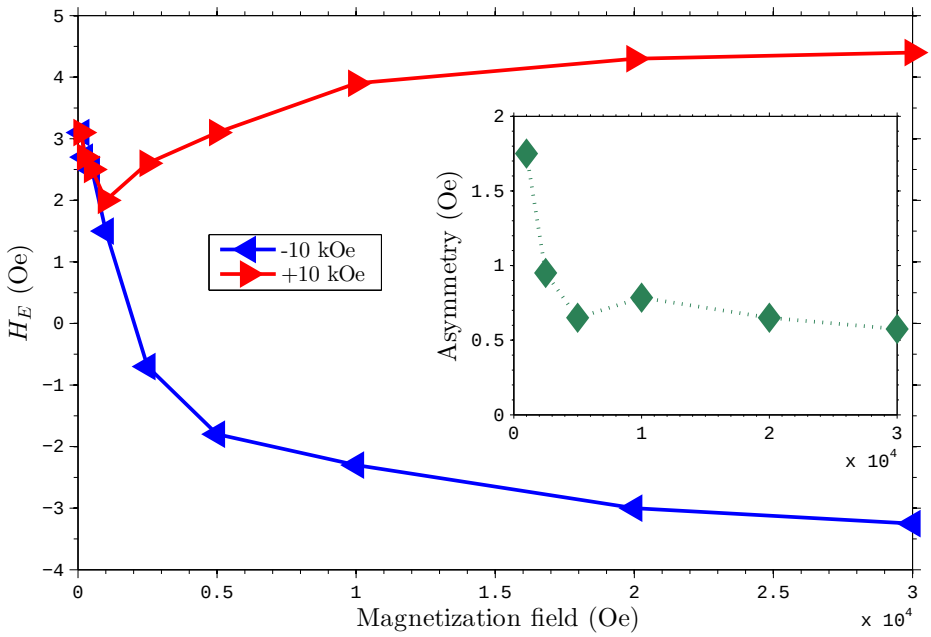


**Figure 5.10:** LSMO (4nm) / Nb:STO Exchange bias after varying sample magnetization at 50 K. Measurements were done with increasing magnetization fields in the range 125 Oe - 30 kOe, and the sample had been exposed to a 20 kOe field prior to the measurements.

The variation of magnetization field shown in figure 5.10 reveals that with magnetization fields under 1000 Oe, the $H_E$ values are similar for both magnetization directions, while for 1000 Oe and above they separate and the separation increases with increasing magnetization field. A change in $H_E$ is also seen for magnetization fields under 1000 Oe, but this may be due to that the sample had been exposed to a 20 kOe field prior to the measurements, and that it is influencing these values. It is thus difficult to conclude anything from the behaviour the measurements done with magnetization fields under 1000 Oe.

However for all magnetization fields of 1000 Oe and above, there is observed an asymmetry similar to that observed at 10 kOe fields for all samples in figure 5.9. The calculated asymmetry for is plotted in the figure 5.10 inset. It seems to level out at approximately 0.6 Oe from the data acquired at highest magnetization fields (5-30 kOe). This may indicate that there are two contributions to the total exchange bias, and that the one which is causing the asymmetry cannot be switched with magnetization fields under 30 kOe - it is always giving a shift of 0.6 Oe. However the shift could also be caused by the VSM having a 0.6 Oe $H$-field offset, which should then be seen in all measurements. All samples show the same asymmetry, as seen in figure 5.9.

Apart from the asymmetry, the other phase which is contributing to exchange bias is giving a shift of up to $\pm 3$ Oe, varying with magnetization field strength. From figure 5.10 it is seen that only magnetization fields above 500 Oe induce a separation of the hystereses. The hysteresis which is observed above $T_C$ in all the samples is found to have a coercive field of roughly 150 Oe and saturate in the range $500 - 1000$ Oe. As it is believed that the

hysteresis is caused by a ferromagnetic phase located in the top layer of the substrate, it is reasonable to suggest that this phase may cause an exchange bias to the LSMO films.

Exchange bias effect has been reported in (001)-oriented LSMO / STO systems, but only significantly for temperatures below 50 K [56, 67]. At 80 K, a value of 10 Oe is found at 80 K - in the same order as the (111) findings - but it rises to 80 Oe at 40 K and are reported to increase for temperatures down to 10 K. Since the values reported are obtained at lower temperatures, it is difficult to compare to the shift seen in the (111)-orientation. However the shift is reported to increase towards low temperatures, in contrast to the tendency seen for some of the (111) films in figure 5.9. This could indicate that the effect observed in the (111) samples may originate from a different origin.

## 5.2 (111) LFO / LSMO / Nb:STO

*In this section the measurement results from the samples with a 4 nm LFO top layer will be presented. Comparison will be done for the samples with the LSMO / Nb:STO films.*

### 5.2.1 Magnetic moment

The temperature dependency of saturation magnetization in the LFO / LSMO / Nb:STO bilayer samples are shown in figure 5.11. Compared to the LSMO / Nb:STO thin films, the samples with a $4\,\mathrm{nm}$ LFO top layer show an increase in magnetic moment for all comparable thicknesses of LSMO (4, 7 and 21 nm). For the samples with thickest LSMO layer (7 and 21 nm) the increase is in the same order of magnitude, while for 4 nm LSMO there is a significantly larger increase. The values at 50 K are summarized in table 5.2. The increase in moment is interesting for all samples since the LFO layer is antiferromagnetic and should not self-evidently contribute to the magnetic moment. The question arises where the additional moment comes from. Especially interesting is the sample with 4 nm LSMO layer. After the subtraction of moment measured at $T_C$, it shows a moment of $4.4\,\mu_\mathrm{B}/\mathrm{Mn}$ at 50 K. This is even higher than the $3.7\,\mu_\mathrm{B}/\mathrm{Mn}$ bulk value of LSMO.

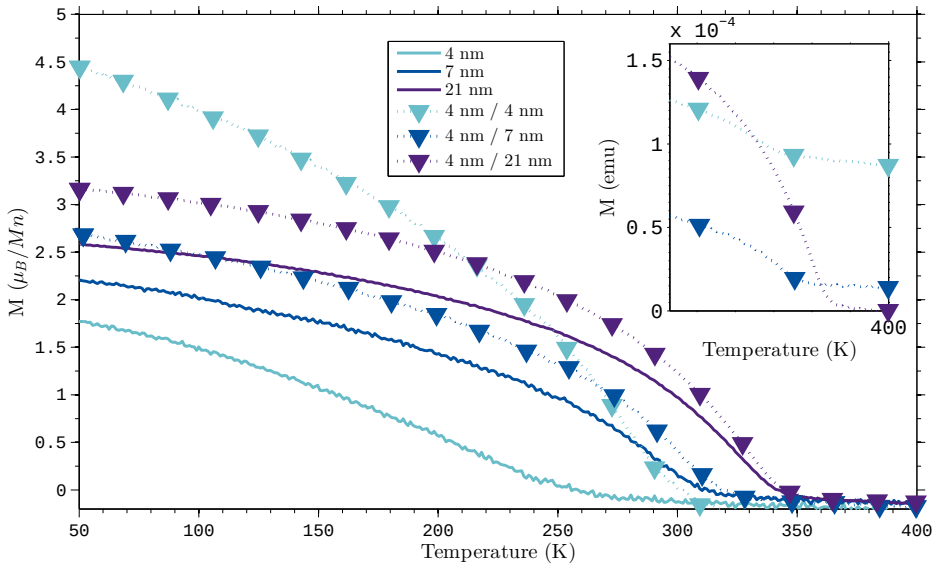


**Figure 5.11:** LFO/LSMO/Nb:STO Moment versus temperature together with measurements from LSMO / Nb:STO samples with comparable LSMO thickness, measured at $H = 2000\,\mathrm{Oe}$ after 20 kOe field cooling from $400\,\mathrm{K}$. All measured data has had the value at $T_C$ subtracted for all temperatures. The figure inset shows the raw data before subtraction.

The magnetic saturation moments measured at 50 K are plotted against LSMO layer thickness (inverse) in figure 5.12, together with the results from the LSMO / Nb:STO film samples. From the figure, the LFO(4nm) / LSMO(4nm) / Nb:STO sample clearly stands out. The two other samples with LFO top layer however indicate a decrease with LSMO thickness, in the same manner as the LSMO / Nb:STO films. When the data from these two samples are extrapolated in the same manner as done with the LSMO / Nb:STO samples, a dead layer thickness close to $1.5\,\mathrm{nm}$ is estimated, similar to the result without an LFO top layer. This could indicate that the LFO layer has not stabilized any parts of the dead layer. However there is an increase in moment, which then could originate from something else than dead layer stabilization.

**Table 5.2:** Measured moments at $50\,\mathrm{K}$. The $\Delta M$ is the difference from the respective thicknesses in LSMO / Nb:STO thin films.

| Sample | Moment($\mu_B$/Mn) | $\Delta M$ |
|---|---|---|
| LFO(4)/LSMO(21)/Nb:STO | 3.2 | 0.5 |
| LFO(4)/LSMO(7)/Nb:STO | 2.7 | 0.6 |
| LFO(4)/LSMO(4)/Nb:STO | 4.4 | 2.7 |

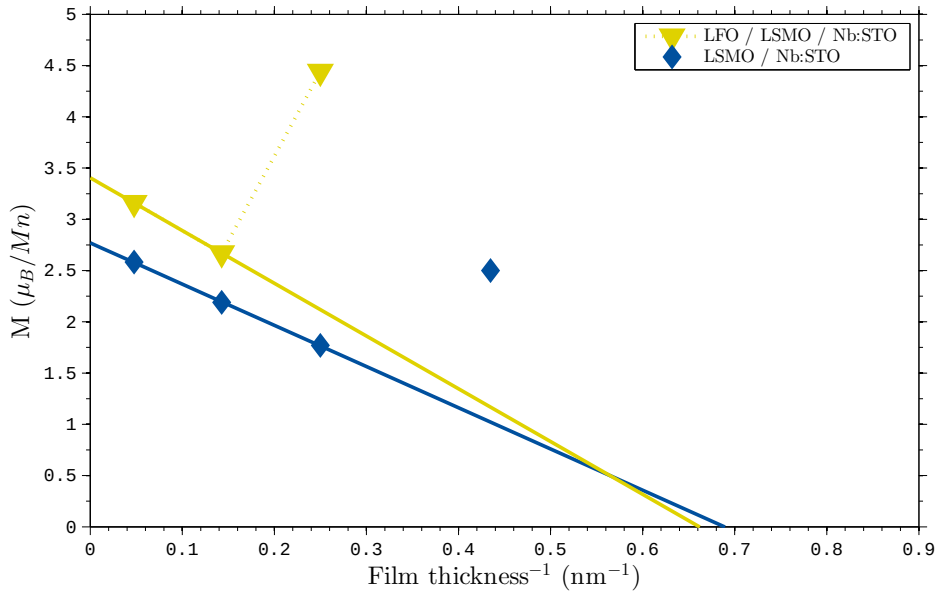


**Figure 5.12:** LFO/LSMO/Nb:STO and LSMO/Nb:STO moments at 50K plotted against inverse thickness of LSMO

The increased moment may be caused by several factors. One interesting suggestion is charge transfer at the interface. As LSMO has continuous $3d$ states from the O $2p$ band an up across the fermi level located $1.5\,\mathrm{eV}$ above, and LFO has a band gap from

the O $2p$ to the upper $3d$ states locted $2.2\,\mathrm{eV}$ above, there are no clear direct indications of electron transfer. However if there are structural changes induced near the interface, which for instance could lead to octahedral tilting, elongation etc., the crystal field splitting and hence the electronic band structures of the materials could be altered. Such transfer may change the magnetic properties of both material layers. If electrons transfer from LFO to LSMO, the increase in moment could for instance be explained by increased spin moment in the LSMO layer, assuming the ferromagnetic phase is conserved. An change in number of electrons could induce significant changes to the orbital structures, and thus also the electronic and magnetic properties. This could lead to observable changes in the hystereses behaviour, for instance by coercive fields or switching sharpness. On the other hand, an change in number of electrons in LFO may also lead to changed magnetic properties there. If electrons are transferred from LSMO to LFO, an additional moment could for instance be explained by an induced ferromagnetic phase in the LFO layer close to the LFO / LSMO interface. Reported calculations on LFO upon such charge transfer indicate a HS - LS transition [38] which would lead to a non-magnetic phase, but the picture may be different if there are structural changes at the (111) interface. Regardless of which direction the charge transfer proceeds, such events have not been reported for the LFO / LSMO system in the (001)- or (110)-orientations. The epitaxial coupling in the (111)-orientation is however expected to be different and possibly yield novel results.

There are also indications of an additional ferromagnetic phase above $T_C$ in the samples with LFO top layer. This can be seen in the figure 5.11 inset for two of the samples - with 4 nm and 7 nm LSMO layers. Scaled to the volume of the substrate, some of the moment values are higher, but still in the same range as the values observed on the LSMO / Nb:STO films. The values are summarized in table 5.3. If the ferromagnetic phase is coming from the substrate, the moment values of $9.5 \cdot 10^{-3}$ emu/cc are around 20 times the value reported on (001) Nb:STO [40].

**Table 5.3:** Measured moments in the LFO / LSMO / Nb:STO samples at $380\,\mathrm{K}$ (above $T_C$), scaled to the volume of the Nb:STO substrate.

| Sample | Moment (emu/cc) |
|---|---|
| LFO / LSMO (4 nm) / Nb:STO | $9.5 \cdot 10^{-3}$ |
| LFO / LSMO (7 nm) / Nb:STO | $1.5 \cdot 10^{-3}$ |
| LFO / LSMO (21 nm) / Nb:STO | $1.3 \cdot 10^{-4}$ |

### 5.2.2 Shift in Curie temperature

An increase in $T_C$ is observed with the addition of the LFO layer. The variations of $T_C$ with thickness is shown in figure 5.13. The change for the two samples with 7 nm and 21 nm LSMO layers is relatively small (7 and 3 K difference), and could be due to error from the $T_C$ estimation method. But the sample with 4 nm LSMO layer has an estimated $T_C$ increase of 43 K. Hence this sample is found to have significant increase in both moment and $T_C$, which likely is correlated. The interaction which is occurring seems to be stabilizing the ferromagnetic phase of the LSMO up to higher temperatures. If there is charge transfer at the interface, it is difficult to anticipate how it will influence the magnetic properties, but increased $T_C$ might be an outcome.

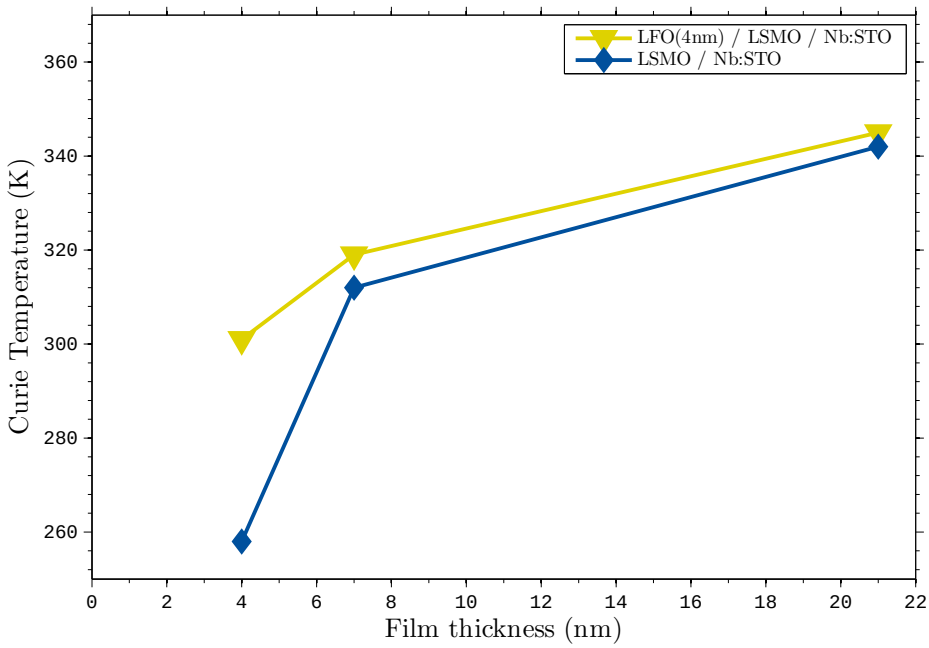


**Figure 5.13:** LFO / LSMO / Nb:STO thickness dependence of $T_C$, plotted together with the results from LSMO / Nb:STO film samples.

### 5.2.3 Hysteresis analysis

*Hystereses are analyzed, and extracted coercive fields and exchange bias values from the samples are compared with corresponding thicknesses of LSMO films in figures 5.14 and 5.15. First the two samples showing relatively similar behaviour to the LSMO / Nb:STO films are discussed, then the LFO (4nm) / LSMO (4nm) /Nb:STO sample which shows the different behaviour.*

The two samples with thickest LSMO layers - 21 nm and 7 nm respectively - show hysteresis behaviour relatively similar to the LSMO / Nb:STO films. Hystereses obtained at 50 K are shown in figure 5.14. The hystereses are comparable to the LSMO / Nb:STO film samples in both moment and coercivity, and the magnetic switching shows similar sharp behaviour by a full switch occuring both ways over roughly 20 Oe. The coercive fields and exchange bias values extracted from these hystereses are shown in figure 5.15 a) and b).

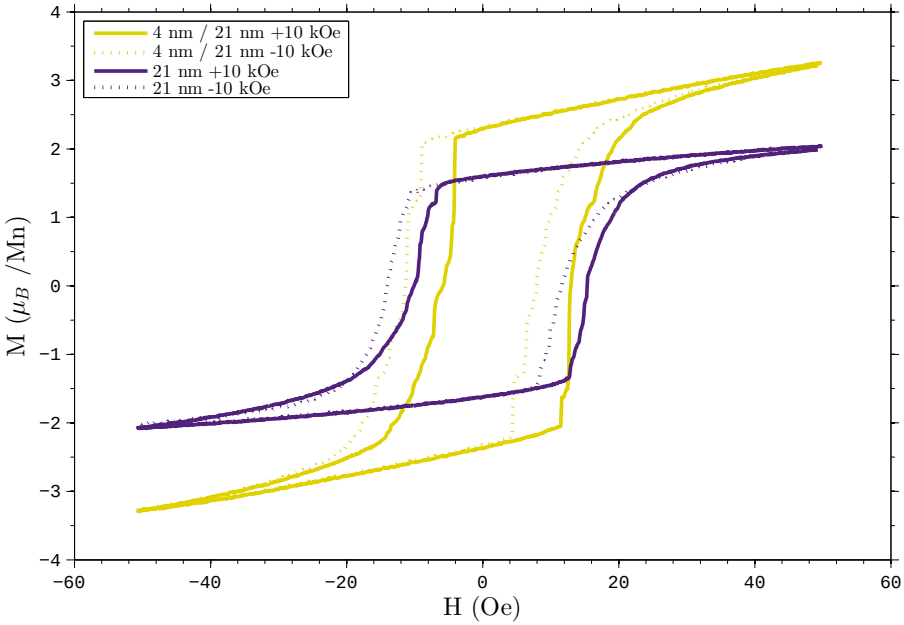


**(a)** 21nm LSMO layer samples

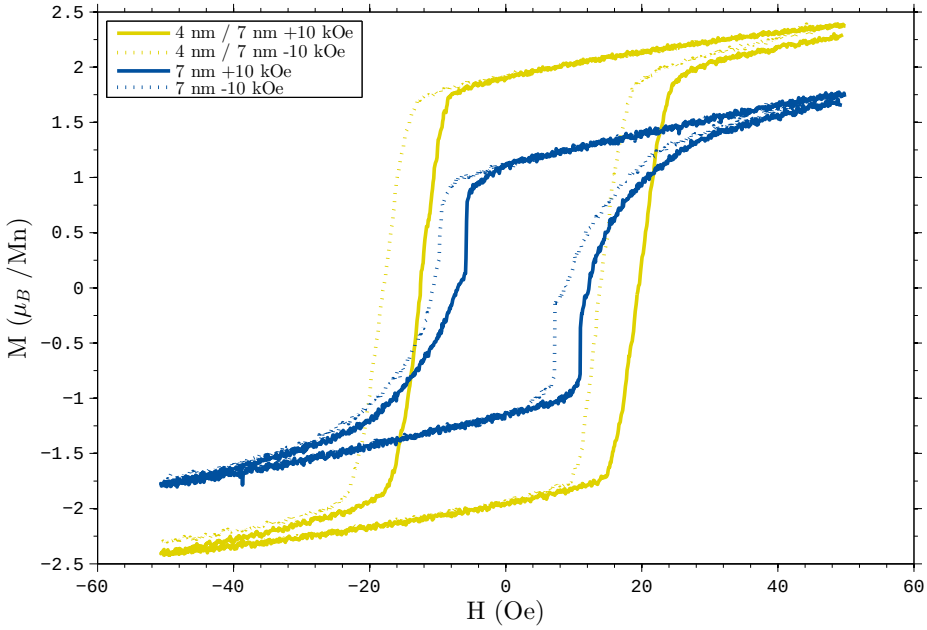


**(b)** 7nm LSMO layer samples

**Figure 5.14:** Hysteresis behaviour at 50 K, obtained after magnetizations in $\pm$10 kOe fields at 50 K

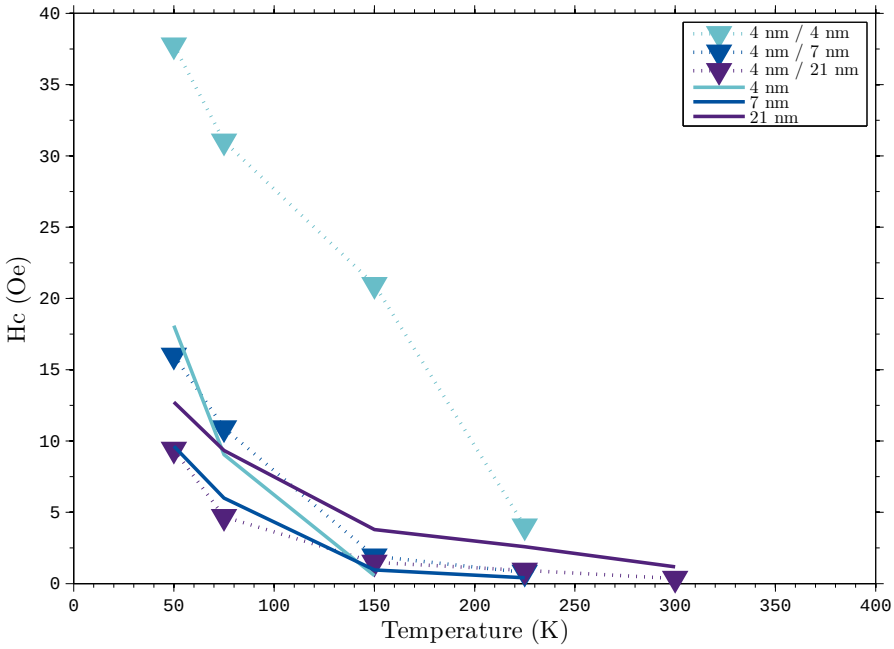


**(a)** $H_C$ vs. Temperature

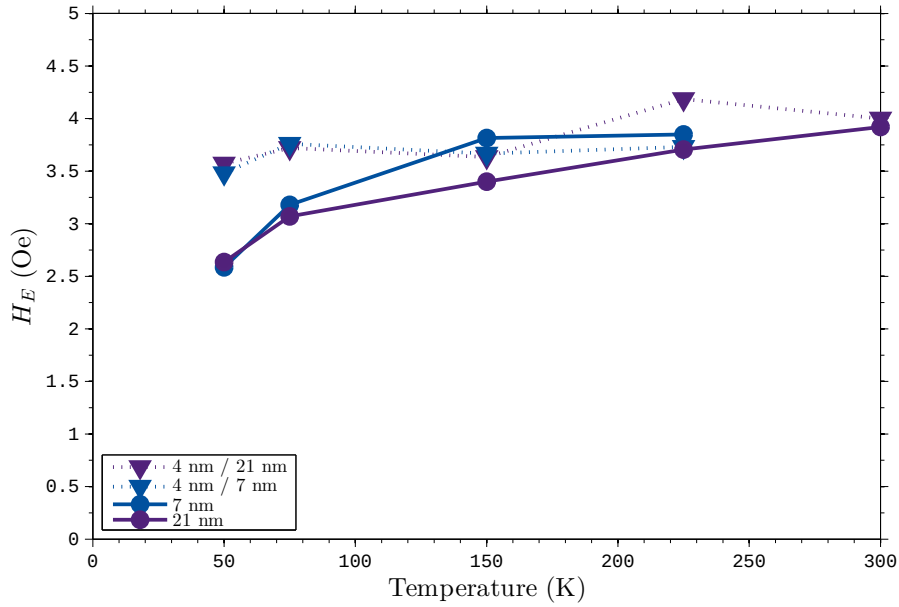


**(b)** $H_E$ vs. Temperature

**Figure 5.15:** Comparison of values obtained from hystereses for LSMO samples with and without 4 nm LFO top layer

With an LFO top layer the coercive field is reduced for the sample with a $21\,\mathrm{nm}$ LSMO layer, but increased for the sample with a $7\,\mathrm{nm}$ LSMO layer. The variations are also small, in the same range (5-6 Oe) similarly to the variations which were found for various thicknesses in the (111) LSMO / Nb:STO samples. As the variations in coercive fields show no specific trend, but vary with both film thickness and temperature within the same order of magnitude, it is difficult to speculate whether the difference observed on the bilayer samples is due to the addition of the LFO top layer or something else, for instance fluctuations that may have occurred during growth procedures.

The temperature behaviour of the exchange bias shown in figure 5.15 may indicate a tendency to decay less towards the lowest temperatures with an LFO top layer, however investigations at temperatures under $50\,\mathrm{K}$ are needed to validate the full temperature behaviour. Since the exchange bias effect is in the same order as observed in the LSMO / Nb:STO samples, its origin is believed to come from the LSMO / Nb:STO system and not being related the LFO top layer. A significant observation is that there is no considerable change in the exchange bias with respect to the presence of an LFO / LSMO interface. An exchange bias is expected due to a fully uncompensated spin surface in the (111) LFO layer.

The shape of the hystereses seen in figure 5.14 give no clear indication of a separate phase for the additional moment, by for instance double loops or other significant changes to the hysteresis shape. The hysteresis loop is found to be simply elongated along the moment-axis. This indicates that the moment comes from a phase which is strongly coupled to the magnetization of the LSMO layer, or that it is the LSMO phase itself. This could for instance fit with the suggestion that charge transfer occurs from LFO to LSMO, giving the ferromagnetic LSMO layer a higher spin number. But the LFO layer then loses electrons,which may cause it to alter properties as well. The LFO / LSMO / Nb:STO samples with 7 and 21 nm LSMO layer do not show clear indications of altered magnetic properties of LFO, but the samples with thinnest (4 nm) LSMO shows severe altered properties.

The hysteresis behaviour of the LFO (4nm) / LSMO (4nm) / Nb:STO sample differs from all the other samples. The hystereses obtained in the temperature range 50-400 K for this sample are shown in figure 5.17, where the figure inset shows the hysteresis at 50 K compared with those from the other two bilayer samples. While the hysteresis loops for the other samples enclose and the moment saturates at about 50 Oe with a value around $\sim 3\,\mu_\mathrm{B}/\mathrm{Mn}$, the sample with 4 nm LSMO layer shows $5\,\mu_\mathrm{B}/\mathrm{Mn}$ at 50 Oe, and saturates at $\sim$12 $\mu_\mathrm{B}/\mathrm{Mn}$ around 2000 Oe. The coercive field was also found to be roughly 2 times larger, and no closed hysteresis loops were found for small field (50 Oe) measurements.

Since the samples with thickest LSMO layers (7 and 21 nm) show typical LSMO hystereses, but the samples with 4 nm LSMO shows a significant change, it may indicate that there is a certain thickness of LSMO somewhere between 4 and 7 nm where the natural LSMO ferromagnetic phase becomes less favoured than an alternative phase which may be induced by interaction at the LSMO / LFO interface, and the result is observed by drastic changes in the ferromagnetic behaviour. A schematic of the proposed event is shown in figure 5.16 . Since a 1.5 nm dead layer is estimated from the LSMO / Nb:STO samples, it could indicate that a 4 nm layer of LSMO is relatively close to its critical thickness, which may make it more susceptible to influence from the LFO / LSMO interface.

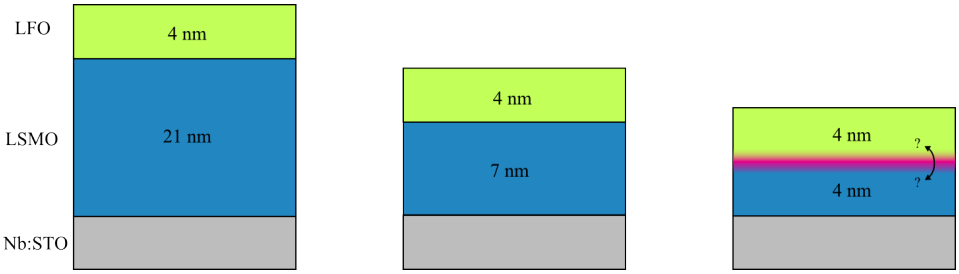


**Figure 5.16:** Schematic showing the onset of significant changes to the ferromagnetic behaviour of LSMO as the film approaches a critical thickness.

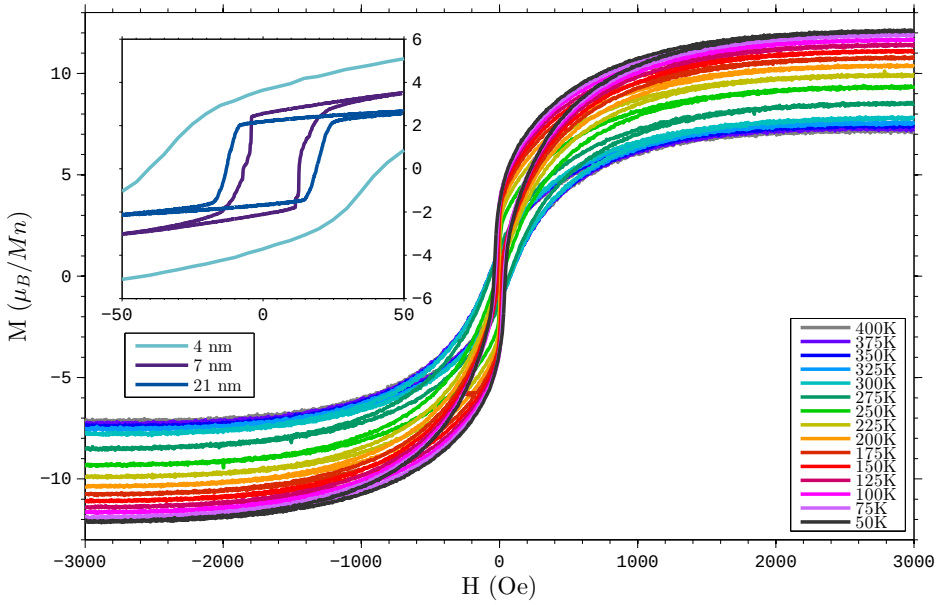


**Figure 5.17:** Hystereses observed from the LFO (4nm) / LSMO (4nm) / Nb:STO sample with $\pm$5000 Oe fields in the temperature range 50-400 K. The figure inset shows the hysteresis at 50 K together with those from the bilayer samples with 7 nm and 21 nm LSMO layers respectively.

There are indications of double loops in the hystereses obtained from the LFO (4nm) / LSMO (4nm) / Nb:STO sample for temperatures under $T_C$, as shown in figure 5.17. Above $T_C$ only one loop is distinguishable. Since the hysteresis observed above $T_C$ could originate from the substrate, and with the assumption that it varies significantly little in the whole temperature range, it was attempted separated out by simple subtraction: The moment measured above $T_C$ was subtracted from the one measured at 50 K. The result is shown in figure 5.18.

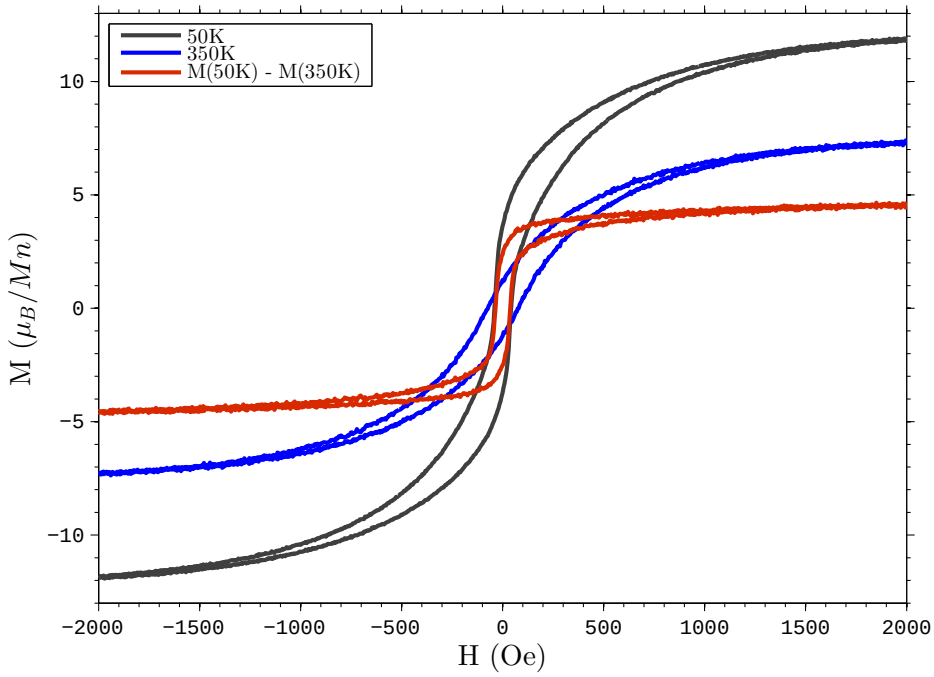


**Figure 5.18:** LFO (4nm) / LSMO (4nm) / Nb:STO hystereses measured at 50 K (under $T_C$), at 350 K (above $T_C$, and the resulting hysteresis wafter subtraction.

The resulting hysteresis after subtraction in figure 5.18 does not show a hysteresis very similar to the ones observed in the LSMO / Nb:STO samples. The hysteresis (red in the figure) encloses well above 500 Oe, the saturation moment is larger than $4\,\mu_B/\mathrm{Mn}$ and the coercive field is still comparable to the one before subtraction. This may indicate two things: The hysteresis observed at 350 K may be changing with temperature and give higher moment at 50 K than at 350 K. But it may also be that the change is due to interaction between LSMO and LFO, and that the red curve in figure 5.18 is showing the result of the interaction - increased moment and coercivity. However the magnetic phases cannot easily be separated out, and the behaviour below $T_C$ should be interpreted as to come from more than one phase. Hence it is difficult to conclude more about the interaction from these results.

## 5.3 (111) LSMO / LFO / Nb:STO

*In this section the results from samples with an underlying LFO layer are presented. As all these samples have an LSMO layer thickness of 4 nm, comparison is mainly done with the other two samples that also have 4 nm LSMO layers, the LSMO (4nm) / Nb:STO and LFO (4nm) / LSMO (4nm) / Nb:STO.*

### 5.3.1 Magnetic moment

An increase in magnetic moment and $T_C$ is found for all bilayer samples with underlying LFO layer. The temperature dependency of the measured moment for varying LFO layer thickness is shown in figure 5.20. In the main figure, the moment has been normalized to be zero at $T_C$ for easier comparison of the variations under $T_C$. The raw data is shown in the figure inset.

The sample with 4 nm LFO underlying layer is found to have a moment of $4.9\,\mu_B/\mathrm{Mn}$ at 50 K, which is an increase of $3.1\,\mu_B/\mathrm{Mn}$ compared to LSMO (4 nm) / Nb:STO. This is higher than the increase of $2.7\,\mu_B/\mathrm{Mn}$ found from the LFO (4nm) / LSMO (4nm) / Nb:STO sample, which has the same layers but the LFO is located on top. Both of these samples have an LFO / LSMO interface, but the one with underlying LFO lacks the LSMO / Nb:STO interface. The difference in moment which seems to occur when simply rearranging the layers could for instance be due to changes in dead layer thickness. Recalling that a magnetic dead layer with estimated thickness of 1.5 nm believed to be located at the LSMO / Nb:STO interface in the LSMO / Nb:STO and possibly similarly in the LFO / LSMO / Nb:STO samples, the dead layer could for instance be smaller when the LSMO / Nb:STO interface is switched out with an LSMO / LFO interface. However the LSMO (4 nm) / LFO (4 nm) / Nb:STO sample's moment of $4.9\,\mu_B/\mathrm{Mn}$ exceeds bulk LSMO values, which indicates that more than just an activation of a dead layer is occurring. A proposed schematic is shown in figure 5.19.

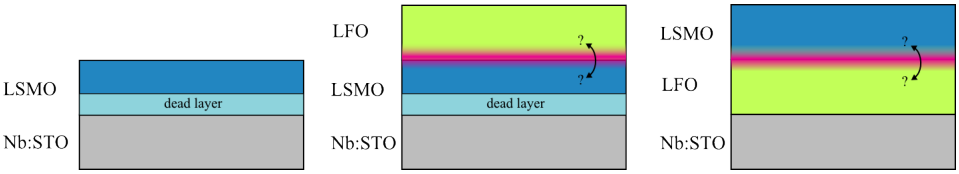


**Figure 5.19:** Schematic showing suggested reduction of the dead layer in LSMO when it is grown on LFO rather than Nb:STO.

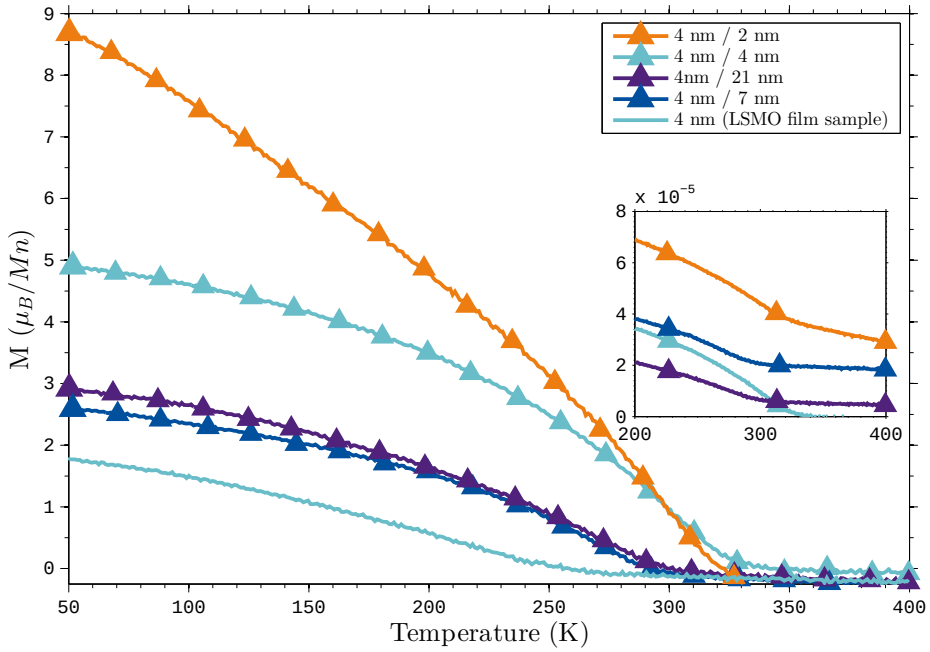


**Figure 5.20:** LSMO/LFO/Nb:STO Moment versus temperature together with the LSMO (4nm) / Nb:STO sample, measured at $H = 2000\,\mathrm{Oe}$ after 20 kOe field cooling from $400\,\mathrm{K}$. All measured data has had the value at $T_C$ subtracted for all temperatures. The figure inset shows the raw data before subtraction.

As seen from the figure 5.20 inset, the curve from the sample with 2 nm LFO layer (orange) shows a decrease in moment as temperature rises even above $T_C$. This indicates that the ferromagnetic phase which is observed above $T_C$, and which is believed to be originating from the substrate, is changing significantly with temperature. This indicates that there could be a larger moment given by this phase at 50 K than at $T_C$, and that the simple subtraction of moment at $T_C$ will yield incorrect values at lower temperatures. By a rough estimation from the curve shape above $T_C$, it seems to have a close to linear dependency with temperature. Assuming that it is linear, an estimation of its contribution to the moment at 50 K was done, shown in figure 5.21.

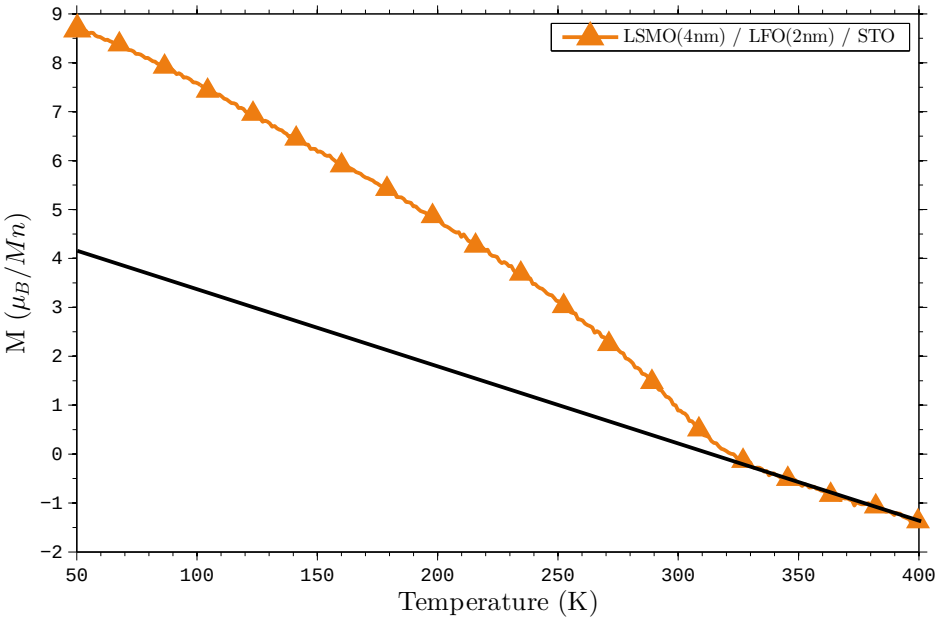


**Figure 5.21:** Estimation of additional moment contribution of a ferromagnetic phase from the substrate at temperatures below $T_C$ for the LSMO (4 nm) / LFO (2 nm) / Nb:STO sample.

The estimation gives a value at 50 K of $4.1\,\mu_B/\mathrm{Mn}$, and when this is subtracted from the value of $8.7\,\mu_B/\mathrm{Mn}$ given by the sample curve (orange), a resulting $4.6\,\mu_B/\mathrm{Mn}$ is obtained. Due to the estimation methods, the value may only be treated as an indication. It is noted that a linear dependency with temperature for the substrate phase is only an assumption. As the behaviour of the moment observed above $T_C$ from the other samples shows close to no temperature dependency, the method was not used on them.

The resulting variation in moment with LFO thickness is shown in figure 5.22, with values obtained at 50 K plotted against LFO thickness. The values are also summarized in table 5.4. The moment from the two samples with thinnest LFO layer (2 and 4 nm) is respectively 4.6 and $4.9\,\mu_B/\mathrm{Mn}$. The suggestion of a reduction of the dead layer thickness is not sufficient to account for these high values, as they surpass the bulk volume magnetization of $3.7\,\mu_B/\mathrm{Mn}$. This suggests changes to the magnetic properties of the LSMO layer, LFO layer , or both.

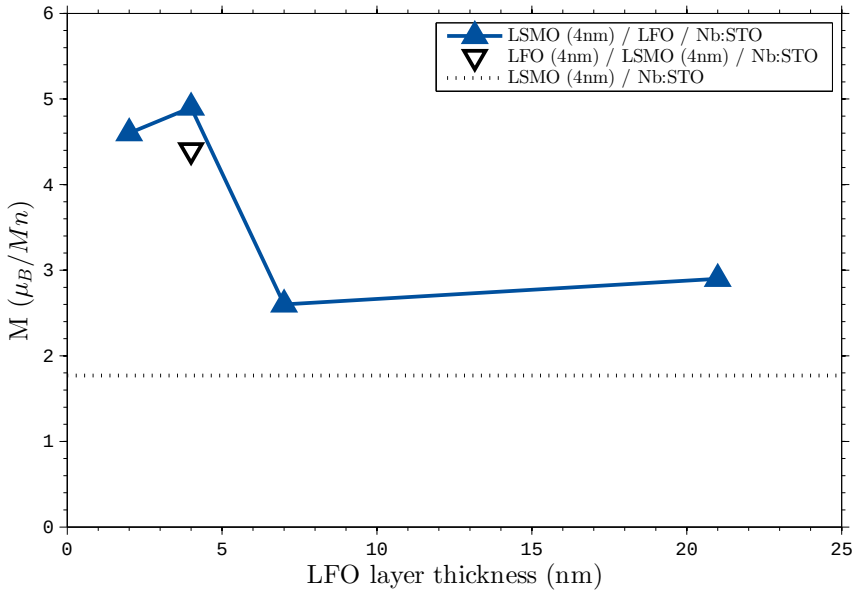


**Figure 5.22:** LSMO/LFO/Nb:STO moments at 50K plotted against inverse thickness of LFO. The reference moment for LSMO (4nm) / Nb:STO is indicated by the blue dotted line.

**Table 5.4:** Measured moments of the LSMO / LFO / Nb:STO samples at 50 K.

| Sample | Moment($\mu_B$/Mn) | $\Delta M$ |
|---|---|---|
| LSMO(4) / Nb:STO (ref) | 1.8 | 0 |
| LSMO(4) / LFO(2) / STO | 4.6 | 2.8 |
| LSMO(4) / LFO(4) / Nb:STO | 4.9 | 3.1 |
| LSMO(4) / LFO(7) / Nb:STO | 2.6 | 0.8 |
| LSMO(4) / LFO(21) / Nb:STO | 2.9 | 1.1 |

### 5.3.2 Shift in Curie temperature

An increase in $T_C$ is observed from the moment versus temperature measurements. The variations in increase for the different samples are shown in figure 5.23 and the values are summarized in table 5.5. Recalling that an increase was also observed for samples with the LFO / LSMO / Nb:STO system, it is likely caused by the presence of the LFO layer, or the LFO / LSMO interface. All the samples presented in figure 5.23 have 4 nm LSMO, but varying LFO layer thickness. The results show that all thicknesses of LFO give an increase in $T_C$, varying in the range 36 - 69 K, and the samples with thinnest LFO layer (2 and 4 nm) show the highest increase. There are striking similarities between the increase in moment and increase in $T_C$, as seen when comparing figures 5.22 and 5.23. This indicates that both changes are highly coupled.

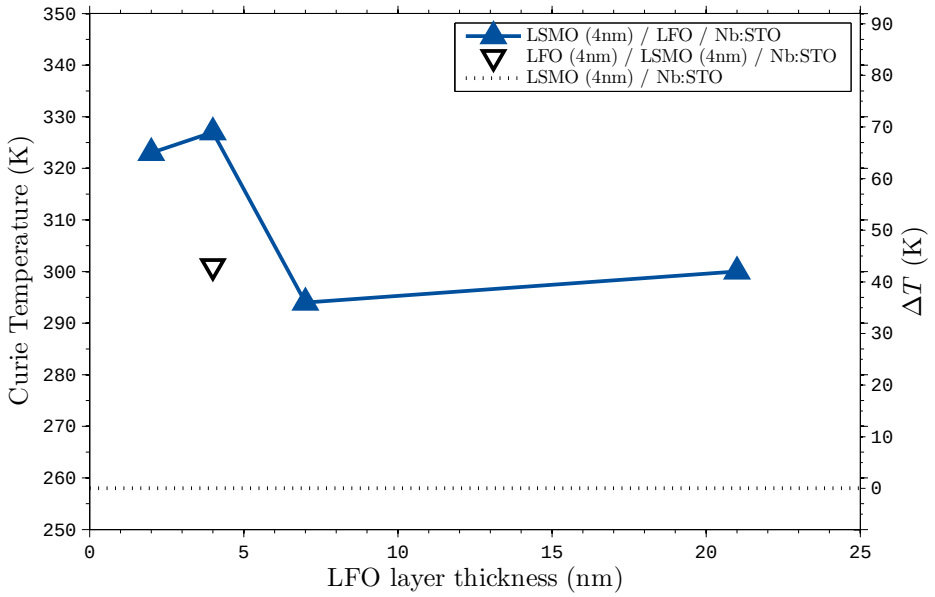


**Figure 5.23:** LSMO / LFO / Nb:STO $T_C$ dependence on LFO layer thickness, plotted together with the two other samples with 4 nm LSMO layer.

**Table 5.5:** $T_C$ values for the samples with 4 nm LSMO layer

| Sample | $T_C$ (K) | $\Delta T$ (K) |
|---|---|---|
| LSMO (4nm) / Nb:STO | 258 | 0 |
| LFO (4nm) / LSMO (4nm) / Nb:STO | 301 | 43 |
| LSMO (4nm) / LFO (2nm) / STO | 323 | 65 |
| LSMO (4nm) / LFO (4nm) / Nb:STO | 327 | 69 |
| LSMO (4nm) / LFO (7nm) / Nb:STO | 294 | 36 |
| LSMO (4nm) / LFO (21nm) / Nb:STO | 300 | 42 |

### 5.3.3 Hysteresis analysis

Hystereses were obtained at temperatures in the range 50 - 400 K. These are shown in figure 5.24 and 5.25. The hystereses observed under $T_C$ differs from the LSMO / Nb:STO film samples, but resemble the behaviour which was seen in the LFO (4nm) / LSMO (4nm) / Nb:STO sample by that they all have increased coercivity and saturation moment, and the magnetic switching occurs over a larger $H$-field interval. There is no sign of exchange bias in any of the samples. Some of the samples show hysteresis loops above $T_C$, which are believed to be originating from the substrate. It is likely that the hystereses from the substrate are part of the ones observed under $T_C$. This should cause double loops under $T_C$ even though they may be hard to spot. The only sample which is believed to show no

trace of the substrate hysteresis is the one with 4 nm LFO layer. It shows no moment or hystereses above $T_C$. Thus the hystereses obtained from this sample are believed to show only the ferromagnetic behaviour of the LSMO layer, the LFO layer and the result of their interactions.

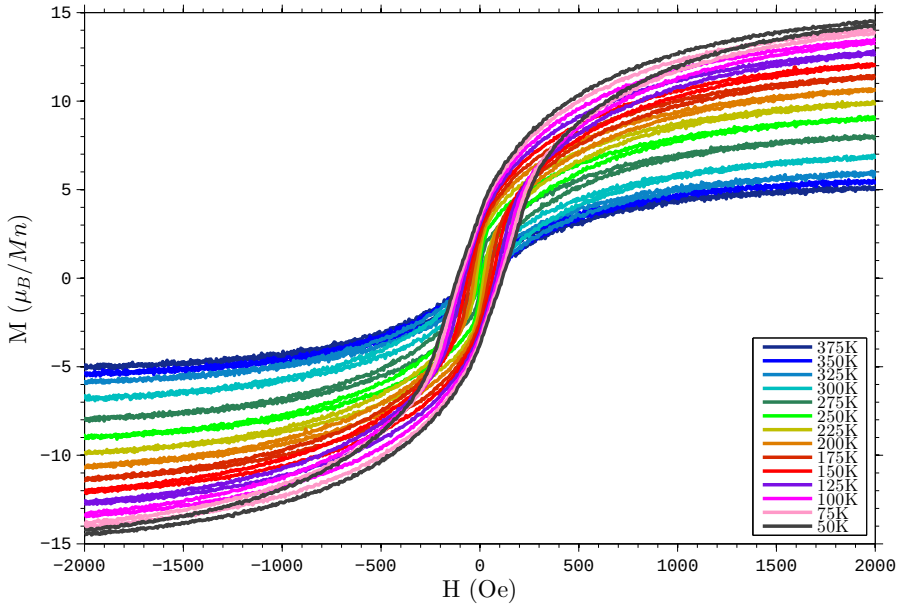


**(a)** 2 nm LFO

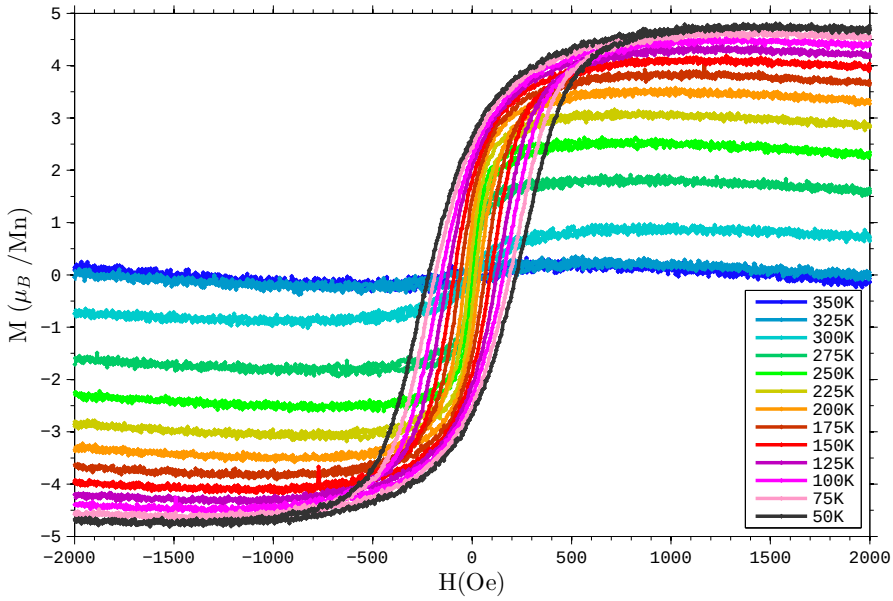


**(b)** 4 nm LFO

**Figure 5.24:** Hysteresis behaviour variations with temperature of the two bilayer samples with 4nm LSMO top layer and thinnest underlying LFO layer. No subtractions have been done to the graphs, but the moments are scaled to the number of Mn atoms in the samples.

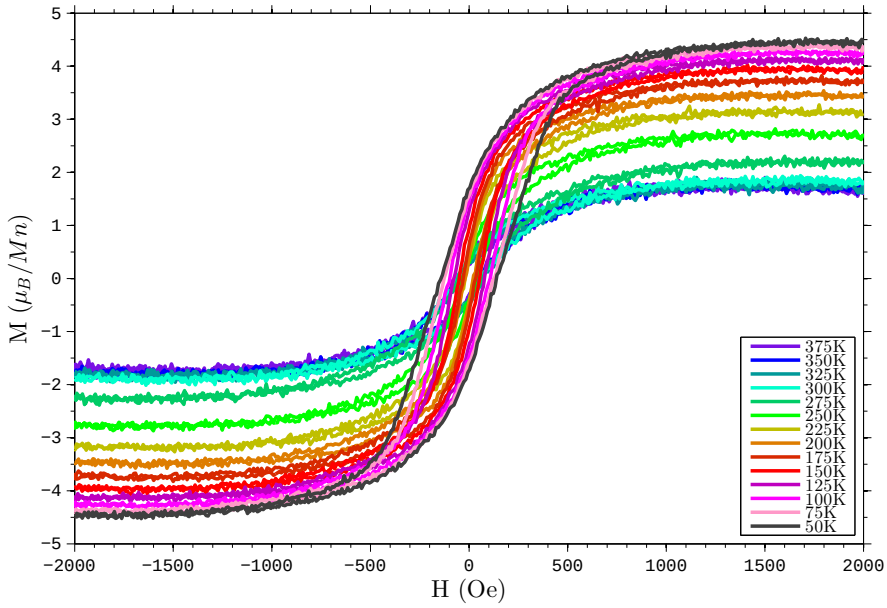


**(a)** 7 nm LFO

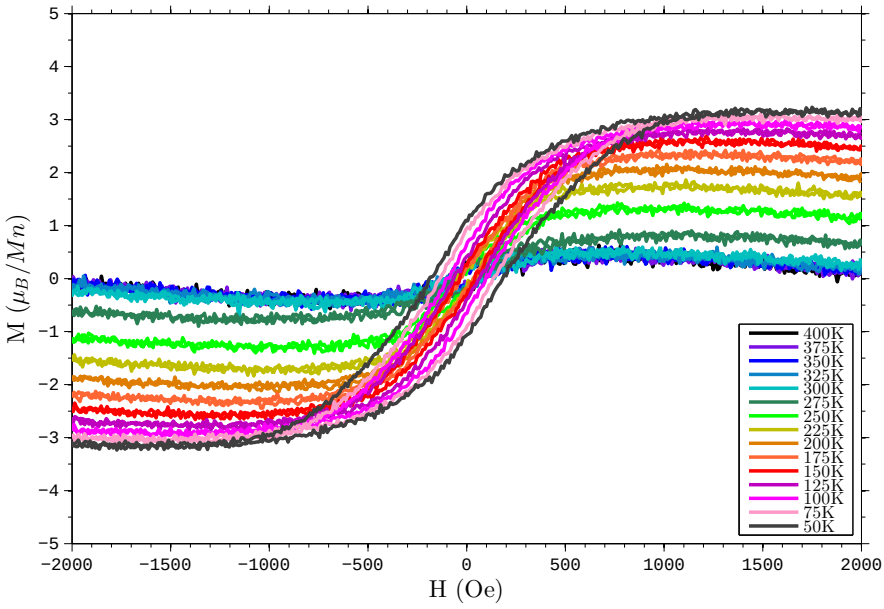


**(b)** 21 nm LFO

**Figure 5.25:** Hysteresis behaviour variations with temperature of the two bilayer samples with 4nm LSMO top layer and thickest underlying LFO layer. No subtractions have been done to the graphs, but the moments are scaled to the number of Mn atoms in the samples.

The typical LSMO hysteresis behaviour, which is observed in the LSMO / Nb:STO film samples with characteristic small coercive fields and sharp magnetic switching, are completely gone from the hystereses seen in figures 5.24 and 5.25. This indicates that the ferromagnetic phase in the LSMO layer has changed properties due to interactions with the LFO layer. If for instance the ferromagnetic phase of LSMO was intact and unchanged, and the changes to moment and coercive fields were originating from a different ferromagnetic phase, there should still be a distinguishable jump in moment at small $H$-fields in the hystereses, indicating the switching of the LSMO phase. However this cannot be observed from the figures. The hystereses are thus believed to show the altered magnetic properties of ferromagnetic LSMO, and possibly induced ferromagnetism in LFO.

Coercive field values were extracted from the hystereses, and the temperature behaviour is plotted in figure 5.26 where the increase relative to LSMO / Nb:STO film samples is clearly seen. The values obtained from the LSMO / LFO / Nb:STO samples at 50 K varies from 114 Oe to 220 Oe, which is a relatively large increase from the 18 Oe observed in the LSMO / Nb:STO sample. Increase in coercivity is known to occur with ferromagnet/antiferromagnet interfaces [53], but there is no clear increase in the LFO / LSMO / Nb:STO samples with LSMO thicknesses of 7 and 21 nm (recall figures 5.14), though these samples also have an LSMO / LFO interface. The increase is however observed in all samples with an LFO / LSMO interface where the LSMO layer is 4 nm. This indicates an interface effect which occurs for thin layers of LSMO only.

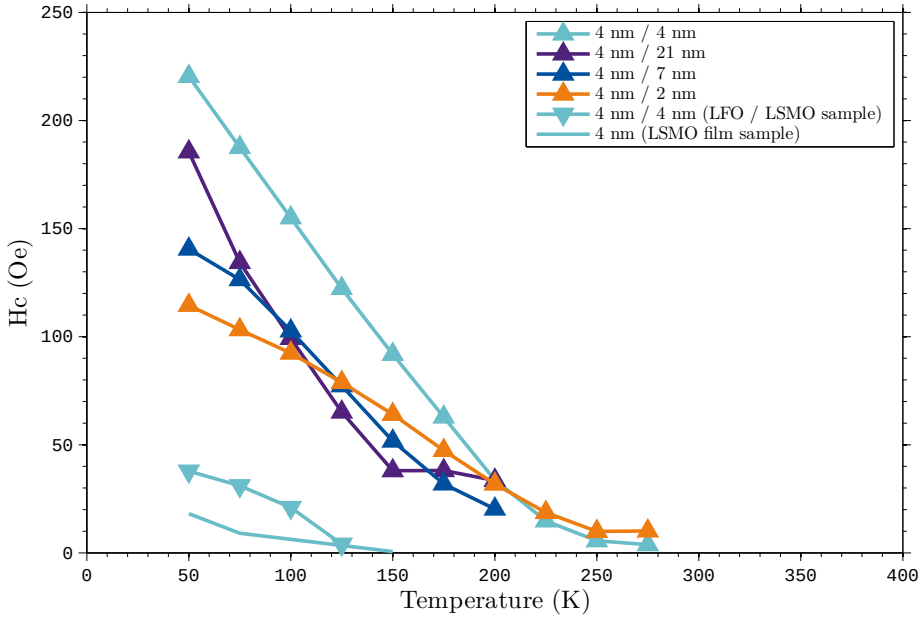


**Figure 5.26:** LSMO / LFO / Nb:STO temperature dependency of the coercive field

Even though there is a large variation in values of coercive fields between the samples

with underlying LFO layer, for instance by comparing the values at 50 K, there is no specific trend observed with LFO layer thickness. At 50 K, the sample with 4 nm LFO layer has the highest $H_C$ value, while the sample with 2 nm LFO has the lowest. A significant observation however, is that the temperature dependency of the coercive field seems to be close to linear. The sample with 4 nm LFO layer, which has no trace of a substrate phase and thus is believed to give most accurate values, has a low increase in $H_C$ right under $T_C$, but it increases linearly from 200 K and down to 50 K, as can be seen from figure 5.26. This differs from the behaviour seen from the LSMO / Nb:STO film samples in figure 5.6, where the temperature dependency is indicated to be exponential. The change is believed to be due to the LFO / LSMO interface interaction, and since there are no signs of exchange bias in any of the samples, a suggestion might be a spin-flop coupling at the interface which causes the increased coercivity.

# 6. Conclusions

Ferromagnetic behaviour of (111)-oriented LSMO / Nb:STO is found to have reduced volume magnetization compared to (001)-oriented films. An indicated magnetic dead layer thickness is however similar to (001) reports. Hysteresis measurements reveal low coercive fields, in an order of magnitude lower than reported (001)-oriented films. The low coercive fields are believed to indicate more freely moving domains in (111)-oriented films than in (001).

A reversable exchange bias effect is found for (111)-oriented LSMO / Nb:STO, with field strength varying with magnetization field. A similar effect is found in the (111) LFO / LSMO / Nb:STO system, for samples with LSMO thickness of 7 and 21 nm, but not for 4 nm. The origin of the bias effect is unknown, and requires more research. No exchange bias effect is found to be induced due to the presence of a (111) LFO / LSMO interface.

An increase in volume magnetization is observed when a layer of LFO is grown either on top or underneath the LSMO layer. The increase is found to be enhanced, and accompanied by increased curie temperature and coercive fields when the LSMO layer is thin (4 nm). The changes are also found to be highest when the LFO layer is thin (2 or 4 nm). The thickness dependence suggests an interface effect, which have not been reported in other crystal orientations. Hence the (111) hexagonal crystallographic structure is indicated to give a different interface environment, inducing novel properties to the functional phases in possibly both material layers.

A ferromagnetic phase additional to the LSMO phase is observed in most of the samples above $T_C$, and is believed to be in correlation with oxygen vacancies, as oxygen annealing is found to reduce the phase.

# Bibliography


[1] F.K. Olsen. Magnetic properties of interfaces in (111)-oriented thin films of $la_{1-x}sr_xmno_3$. December 2013.

[2] M. Quirk and J. Serda. *Semiconductor Manufacturing Technology*. Prentice-Hall, Upper Saddle River, New Jersey 07458, 2001.

[3] H. Y. Hwang, Y. Iwasa, M. Kawasaki, B. Keimer, N. Nagaosa, and Y. Tokura. Emergent phenomena at oxide interfaces. *Nat Mater*, 11(2):103–13, 2012. Hwang, H Y Iwasa, Y Kawasaki, M Keimer, B Nagaosa, N Tokura, Y eng England 2012/01/25 06:00 Nat Mater. 2012 Jan 24;11(2):103-13. doi: 10.1038/nmat3223.

[4] Darrell G. Schlom, Long-Qing Chen, Xiaoqing Pan, Andreas Schmehl, and Mark A. Zurbuchen. A thin film approach to engineering functionality into oxides. *Journal of the American Ceramic Society*, 91(8):2429–2454, 2008.

[5] Shriram Ramanathan (Ed.). *Thin Film Metal-Oxides: Fundamentals and Applications in Electronics and Energy*. Springer, New York, NY 10013, USA, 2010.

[6] David V. Taylor and Dragan Damjanovic. Piezoelectric properties of rhombohedral pb(zr,Łti)o3 thin films with (100), (111), and random crystallographic orientation. *Applied Physics Letters*, 76(12):1615, 2000.

[7] Jung Chang Uk. Tuning of the ferromagnetic properties in $srruo_3$ thin films. *Journal of the Korean Physical Society*, 58(1):83, 2011.

[8] J. Q. Wang, R. C. Barker, G. J. Cui, T. Tamagawa, and B. L. Halpern. Doped rare-earth perovskite mn films with colossal magnetoresistance. *Applied Physics Letters*, 71(23):3418, 1997.

[9] H. Zheng, J. Wang, S. E. Lofland, Z. Ma, L. Mohaddes-Ardabili, T. Zhao, L. Salamanca-Riba, S. R. Shinde, S. B. Ogale, F. Bai, D. Viehland, Y. Jia, D. G. Schlom, M. Wuttig, A. Roytburd, and R. Ramesh. Multiferroic batio3-cofe2o4 nanostructures. *Science*, 303(5658):661–663, 2004.

[10] M. Bowen, M. Bibes, A. Barthelemy, J. P. Contour, A. Anane, Y. Lematre, and A. Fert. Nearly total spin polarization in la2/3sr1/3mno3 from tunneling experiments. *Applied Physics Letters*, 82(2):233, 2003.

[11] Sourabh Jain, Himanshu Sharma, Amit Kumar Shukla, C. V. Tomy, V. R. Palkar, and Ashwin Tulapurkar. Optimization of la0.7sr0.3mno3 thin film by pulsed laser deposition for spin injection. *Physica B: Condensed Matter*, 448:103–106, 2014.

[12] J. Löning, F. Nolting, A. Scholl, H. Ohldag, J. Seo, J. Fompeyrine, J. P. Locquet, and J. Sthr. Determination of the antiferromagnetic spin axis in epitaxial lafeo3 films by x-ray magnetic linear dichroism spectroscopy. *Physical Review B*, 67(21), 2003.

[13] I. Hallsteinsen, J. E. Boschker, M. Nord, S. Lee, M. Rzchowski, P. E. Vullum, J. K. Grepstad, R. Holmestad, C. B. Eom, and T. Tybell. Surface stability of epitaxial la0.7sr0.3mno3 thin films on (111)-oriented srtio3. *Journal of Applied Physics*, 113(18):183512, 2013.

[14] I.R. Shein, K.I. Shein, V.L. Kozhevnikov, and A.L. Ivanovskii. Band structure and the magnetic and elastic properties of srfeo3 and lafeo3 perovskites. *Physics of the Solid State*, 47(11):2082–2088, 2005.

[15] A. West. *Basic Solid State Chemistry*. Wiley, New York, USA, 1999.

[16] E. Schrödinger. An undulatory theory of the mechanics of atoms and molecules. *Phys. Rev.*, 28:1049–1070, Dec 1926.

[17] P. Zeeman. On the influence of magnetism on the nature of the light emitted by a substance. *Astrophysical Journal*, 5(1):332, 1897.

[18] N.A. Spaldin. *Magnetic Materials: Fundamentals and Applications*. Cambridge University Press, New York, USA, 2011.

[19] M. Mansfield and C. O'Sullivan. *Understanding Physics*. Wiley, Chichester, UK, 2011.

[20] R.J. Tilley. *Understanding Solids: The Science of Materials*. John Wiley & Sons, Inc., Chinchester, UK, 2004.

[21] C. Kittel. *Introduction to Solid State Physics*. Wiley, New York, USA, 2005.

[22] C. Kittel. Theory of the structure of ferromagnetic domains n films and small particles. *J. Phys. Rev.*, 70(11 & 12):965–971, 1946.

[23] S. Prosandeev, S. Lisenkov, and L. Bellaiche. Kittel law in $bifeo_3$ ultrathin films: A first-principles-based study. *Physical Review Letters*, 105(14), 2010.

[24] V.M. Goldschmidt. Die gesetze der krystallochemie. *Naturwissenschaften*, 14(21):477–485, 1926.

[25] K. Singh, S. Acharya, and D. V. Atkare. Qualitative analysis of tolerance factor, electronegativity and chemical bonding of some ferroelectric perovskites through mot. *Ferroelectrics*, 315(1):91–110, 2005.

[26] Nicole A. Benedek and Craig J. Fennie. Why are there so few perovskite ferroelectrics? *The Journal of Physical Chemistry C*, 117(26):13339–13349, 2013.

[27] Elbio Dagotto, Takashi Hotta, and Adriana Moreo. Colossal magnetoresistant materials: the key role of phase separation. *Physics Reports*, 344(13):1 – 153, 2001.

[28] A. Urushibara, T. Arima, A. Asamitsu, G. Kido, and Y. Tokura. Insulator-metal transition and giant magnetoresistance in $la_{1-x}sr_xmno_3$. *Physical Review B*, 51(20):14103–14109, 1995.

[29] Francis S. Galasso and Michael Kestigan. *Barium Titanate, BaTiO3*, pages 142–143. John Wiley & Sons, Inc., 2007.

[30] Hiroyuki Fujishiro, Tetsuo Fukase, and Manabu Ikebe. Charge ordering and sound velocity anomaly in $la_{1-X}sr_xmno_3$ ($x > 0.5$). *Journal of the Physical Society of Japan*, 67(8):2582–2585, 1998.

[31] A. Khapikov, L. Uspenskaya, I. Bdikin, Ya Mukovskii, S. Karabashev, D. Shulyaev, and A. Arsenov. Magnetic domains and twin structure of the la0.7sr0.3mno3 single crystal. *Applied Physics Letters*, 77(15):2376, 2000.

[32] Takao Kotani and Hiori Kino. Re-examination of half-metallic ferromagnetism for doped lamno 3 in a quasiparticle self-consistent gw method. *Journal of Physics: Condensed Matter*, 21(26):266002, 2009.

[33] M. Konoto, T. Kohashi, K. Koike, T. Arima, Y. Kaneko, Y. Tomioka, and Y. Tokura. Magnetic domain structure of a la0.7sr0.3mno3(001) surface observed by a spin-polarized scanning electron microscope. *Applied Physics Letters*, 84(13):2361, 2004.

[34] Zhongqin Yang, Zhong Huang, Ling Ye, and Xide Xie. Influence of parameters u and j in the lsda + u method on electronic structure of the perovskites $lamo_3$(m=cr,mn,fe,co,ni). *Phys. Rev. B*, 60:15674–15682, Dec 1999.

[35] W.C. Koehler and E.O. Wollan. Neutron-diffraction study of the magnetic properties of perovskite-like compounds labo3. *Journal of Physics and Chemistry of Solids*, 2(2):100 – 106, 1957.

[36] Selma Erat, Artur Braun, Cinthia Piamonteze, Zhi Liu, Alejandro Ovalle, Hansjrgen Schindler, Thomas Graule, and Ludwig J. Gauckler. Entanglement of charge transfer, hole doping, exchange interaction, and octahedron tilting angle and their influence on the conductivity of la1xsrxfe0.75ni0.25o3: A combination of x-ray spectroscopy and diffraction. *Journal of Applied Physics*, 108(12):–, 2010.

[37] J. Zaanen, G. Sawatzky, and J. Allen. Band gaps and electronic structure of transition-metal compounds. *Physical Review Letters*, 55(4):418–421, 1985.

[38] J.E. Kleibeuker, Z. Zhong, H. Nishikawa, J. Gabel, A. Müller, F. Pfaff, M. Sing, K. Held, R. Claessen, G. Koster, and G. Rijnders. Electronic reconstruction at the isopolar $\mathrm{latio_3/lafeo_3}$ interface: An x-ray photoemission and density-functional theory study. *Phys. Rev. Lett.*, 113:237402, Dec 2014.

[39] Takeshi Tomio, Hidejiro Miki, Hitoshi Tabata, Tomoji Kawai, and Shichio Kawai. Control of electrical conductivity in laser deposited srtio3 thin films with nb doping. *Journal of Applied Physics*, 76(10):5886, 1994.

[40] Z. Q. Liu, W. M. Lü, S. L. Lim, X. P. Qiu, N. N. Bao, M. Motapothula, J. B. Yi, M. Yang, S. Dhar, T. Venkatesan, and Ariando. Reversible room-temperature ferromagnetism in nb-doped srtio$_3$ single crystals. *Phys. Rev. B*, 87:220405, Jun 2013.

[41] F. Tsui, M. C. Smoak, T. K. Nath, and C. B. Eom. Strain-dependent magnetic phase diagram of epitaxial la0.67sr0.33mno3 thin films. *Applied Physics Letters*, 76(17):2421, 2000.

[42] P. Perna, C. Rodrigo, E. Jimnez, F. J. Teran, N. Mikuszeit, L. Mchin, J. Camarero, and R. Miranda. Tailoring magnetic anisotropy in epitaxial half metallic la0.7sr0.3mno3 thin films. *Journal of Applied Physics*, 110(1):–, 2011.

[43] Y. Suzuki, H. Y. Hwang, S. W. Cheong, and R. B. van Dover. The role of strain in magnetic anisotropy of manganite thin films. *Applied Physics Letters*, 71(1):140, 1997.

[44] L. M. Berndt, Vincent Balbarin, and Y. Suzuki. Magnetic anisotropy and strain states of (001) and (110) colossal magnetoresistance thin films. *Applied Physics Letters*, 77(18):2903–2905, 2000.

[45] H.-U. Habermeier. Substrate surface engineering for functional ceramic thin film growth. *Journal of Electroceramics*, 13(1-3):23–27, 2004.

[46] Rajesh Chopdekar, Elke Arenholz, and Y. Suzuki. Orientation and thickness dependence of magnetization at the interfaces of highly spin-polarized manganite thin films. *Physical Review B*, 79(10), 2009.

[47] Å smund Monsen, Jos E. Boschker, Ferran Maci, Justin W. Wells, Per Nordblad, Andrew D. Kent, Roland Mathieu, Thomas Tybell, and Erik Wahlstrm. Thickness dependence of dynamic and static magnetic properties of pulsed laser deposited la0.7sr0.3mno3 films on srtio3(001). *Journal of Magnetism and Magnetic Materials*, 369:197–204, 2014.

[48] H. Kumigashira, A. Chikamatsu, R. Hashimoto, M. Oshima, T. Ohnishi, M. Lippmaa, H. Wadati, A. Fujimori, K. Ono, M. Kawasaki, and H. Koinuma. Robust ti4+ states in srtio3 layers of la0.6sr0.4mnosubsrtio3la0.6sr0.4mno3 junctions. *Applied Physics Letters*, 88(19):192504, 2006.

[49] Flavio Y Bruno, Javier Garcia-Barriocanal, M Varela, NM Nemes, P Thakur, JC Cezar, NB Brookes, A Rivera-Calzada, M Garcia-Hernandez, C Leon, et al. Electronic and magnetic reconstructions in la0.7sr0.3mno3/srtio3 heterostructures: A case of enhanced interlayer coupling controlled by the interface. *Physical review letters*, 106(14):147205, 2011.

[50] Hans Boschker, Jaap Kautz, Evert P. Houwman, Gertjan Koster, Dave H. A. Blank, and Guus Rijnders. Magnetic anisotropy and magnetization reversal of la[sub 0.67]sr[sub 0.33]mno[sub 3] thin films on srtio[sub 3](110). *Journal of Applied Physics*, 108(10):103906, 2010.

[51] A. Ruotolo, A. Oropallo, F. Miletto Granozio, G. P. Pepe, P. Perna, and U. Scotti di Uccio. Magnetic and magnetotransport properties of la0.7sr0.3mno3/permalloy heterostructures. *Applied Physics Letters*, 88(25):252504, 2006.

[52] I. Hallsteinsen, E. Folven, F.K. Olsen, R.V. Chopdekar, M.S. Rzchowski, C.B. Eom, J.K. Grepstad, and T. Tybell. Crystalline symmetry controlled magnetic switching in epitaxial (111) la0.7sr0.3mno3 thin films. *Applied Physics Letters (Accepted)*.

[53] J Nogus and Ivan K Schuller. Exchange bias. *Journal of Magnetism and Magnetic Materials*, 192(2):203 – 232, 1999.

[54] Yayoi Takamura, Erik Folven, Jonathan B. R. Shu, Karl R. Lukes, Binzhi Li, Andreas Scholl, Anthony T. Young, Scott T. Retterer, Thomas Tybell, and Jostein K. Grepstad. Spin-flop coupling and exchange bias in embedded complex oxide micromagnets. *Phys. Rev. Lett.*, 111:107201, Sep 2013.

[55] T. C. Schulthess and W. H. Butler. Consequences of spin-flop coupling in exchange biased films. *Phys. Rev. Lett.*, 81:4516–4519, Nov 1998.

[56] S. J. Zhu, J. Yuan, B. Y. Zhu, F. C. Zhang, B. Xu, L. X. Cao, X. G. Qiu, B. R. Zhao, and P. X. Zhang. Exchange bias effect and enhanced magnetoresistance in la0.67sr0.33mno3/srtio3 superlattices. *Applied Physics Letters*, 90(11):112502, 2007.

[57] D. Schumacher, A. Steffen, J. Voigt, J. Schubert, Th. Brückel, H. Ambaye, and V. Lauter. Inducing exchange bias in $la_{0.67}sr_{0.33}mno_{3-\delta}$/$srtio_3$ thin films by strain and oxygen deficiency. *Phys. Rev. B*, 88:144427, Oct 2013.

[58] C.A. Schneider, W.S. Rasband, and K.W. Eliceiri. Nih image to imagej: 25 years of image analysis. *Nature Methods*, 9:671–675, 2012.

[59] Quantum design, 6325 Lusk Boulevard, San Diego, CA 92121, USA. *VersaLab free User's Manual*, fifth edition, february 2013.

[60] A. J. Millis, T. Darling, and A. Migliori. Quantifying strain dependence in colossal magnetoresistance manganites. *Journal of Applied Physics*, 83(3):1588, 1998.

[61] M. Huijben, L. W. Martin, Y. H. Chu, M. B. Holcomb, P. Yu, G. Rijnders, D. H. A. Blank, and R. Ramesh. Critical thickness and orbital ordering in ultrathin $la_{0.7}sr_{0.3}mno_3$ films. *Physical Review B*, 78(9), 2008.

[62] R. P. Borges, W. Guichard, J. G. Lunney, J. M. D. Coey, and F. Ott. Magnetic and electric dead layers in (la0.7sr0.3)mno3 thin films. *Journal of Applied Physics*, 89(7):3868, 2001.

[63] R. Peng, H.C. Xu, M. Xia, J.F. Zhao, X. Xie, D.F. Xu, B.P. Xie, and D.L. Feng. Tuning the dead-layer behavior of la0.67sr0.33mno3/srtio3 via interfacial engineering. *Applied Physics Letters*, 104(8):081606–081606–5, Feb 2014.

[64] Bongju Kim, Daeyoung Kwon, Jong Hyun Song, Yasuyuki Hikita, Bog G. Kim, and Harold Y. Hwang. Finite size effect and phase diagram of ultra-thin la0.7sr0.3mno3. *Solid State Communications*, 150(13-14):598–601, 2010.

[65] Y. F. Tian, J. F. Ding, W. N. Lin, Z. H. Chen, A. David, M. He, W. J. Hu, L. Chen, and T. Wu. Anomalous exchange bias at collinear/noncollinear spin interface. *Scientific Reports*, 3, 2013.

[66] M. Ziese, I. Vrejoiu, A. Setzer, A. Lotnyk, and D. Hesse. Coupled magnetic and structural transitions in la0.7sr0.3mno3films on srtio3. *New Journal of Physics*, 10(6):063024, 2008.

[67] D. Schumacher. *Interplay between magnetic and dielectric phenomena at transition metal oxide interfaces*. PhD thesis, Aachen University, 2012.